STM JOURNALS

Journal of
Materials & Metallurgical Engineering

ISSN: 2231-3818 (Online)
ISSN: 2321-4236 (Print)
Volume 16, Issue 3, 2026
September–December
DOI (Journal): 10.37591/JoMME

https://journals.stmjournals.com/jomme

Review JoMME

# A Nonlinear Galerkin Reduced-Order Model for Liquid Jet Breakup Dynamics and Satellite Droplet Formation

Lakshmi. N. Sridhar

***Abstract***

*Liquid jet breakup is a complex nonlinear free-surface phenomenon governed by the coupled effects of inertia, viscosity, and surface tension. Accurate prediction of jet evolution and satellite droplet formation remains challenging due to the computational cost associated with resolving rapidly evolving interfaces and multiscale breakup dynamics. In this work, a physics-based Galerkin reduced-order model is developed to describe the nonlinear dynamics of liquid jets using a low-dimensional representation of the interface deformation and axial velocity fields. The governing slender-jet equations are nondimensionalized and projected onto a finite set of spatial modes, yielding a six-state nonlinear dynamical system comprising three radius-deformation modes and three velocity modes. The formulation preserves the essential physical mechanisms of capillary restoration, viscous dissipation, nonlinear geometric deformation, and mode-to-mode interaction responsible for the evolution of jet instabilities. The reduced-order model provides an efficient framework for analyzing the nonlinear behavior of liquid jets while maintaining a direct connection with the underlying fluid mechanics. The model captures the coupled evolution of interface and velocity fluctuations and provides a computationally efficient alternative to high-fidelity simulations for exploring breakup dynamics. The proposed framework establishes a foundation for advanced stability analysis and physics-based manipulation of liquid jet breakup and satellite droplet formation.*

**Keywords:** liquid jet breakup; reduced-order modeling; Galerkin projection; capillary instability; satellite droplets; nonlinear free-surface dynamics.

## INTRODUCTION

Liquid jets are among the most fundamental examples of nonlinear free-surface flows and play a central role in numerous natural and engineering systems, including spray atomization, fuel injection, inkjet printing, microfluidic droplet generation, and pharmaceutical processing. In these applications, the transition from a continuous liquid column into discrete droplets is governed by a complex interplay between inertia, viscosity, and surface tension. Although the basic mechanisms responsible for jet breakup have been studied extensively, predicting and controlling the nonlinear evolution of liquid jets remains a challenging problem due to the multiscale nature of the underlying dynamics. The breakup process involves the amplification of small interface disturbances, nonlinear deformation of the liquid column, formation of thinning neck regions, and eventual pinch-off accompanied by the generation of primary and satellite droplets.

The dynamics preceding breakup are particularly important because they determine the final droplet size distribution, breakup length, and satellite droplet production. While direct numerical simulations based on the full free-surface Navier–Stokes equations can provide detailed descriptions

***Author for Correspondence**
Lakshmi. N. Sridhar
E-mail: hkravuri32@gmail.com

Professor, Department of Chemical Engineering. University of Puerto Rico Mayagüez, Puerto Rico, United States of America, United States

Received Date: August 07, 2026
Accepted Date: September 07, 2026
Published Date: October 29, 2026

**Citation:** Lakshmi. N. Sridhar. A Nonlinear Galerkin Reduced-Order Model for Liquid Jet Breakup Dynamics and Satellite Droplet Formation. Journal of Materials & Metallurgical Engineering. 2026; 16(3): 34–66p.

© STM Journals 2026. All Rights Reserved 

of interface evolution, they require significant computational resources because they must resolve rapidly changing geometries, moving boundaries, and small-scale features near pinch-off. These computational requirements make high-fidelity simulations unsuitable for repeated parameter studies, real-time prediction, and design-oriented investigations. Consequently, reduced-order modeling approaches have become increasingly attractive because they provide compact representations of complex fluid systems while preserving the dominant physical mechanisms.

For liquid jets, an effective reduced-order model must capture the essential coupling between interface deformation and internal flow dynamics. The evolution of the jet radius is not independent of the axial velocity field; rather, deformation modifies the flow distribution, and the resulting velocity fluctuations further influence the interface evolution. This nonlinear feedback mechanism controls the growth, saturation, and interaction of capillary modes responsible for jet breakup. Therefore, a reduced-order description based solely on geometric evolution or linear instability assumptions is insufficient for representing the strongly nonlinear dynamics occurring before droplet formation.

Galerkin projection methods provide a systematic framework for constructing reduced-order representations by expressing the evolving interface and velocity fields as combinations of spatial basis functions. By retaining a finite number of dominant modes, the infinite-dimensional free-surface problem can be transformed into a low-dimensional nonlinear dynamical system. Such a representation provides direct access to the modal interactions governing the evolution of the jet and enables efficient exploration of parameter-dependent dynamics. However, developing a reduced-order model that simultaneously preserves physical consistency, nonlinear coupling, and computational efficiency remains a significant challenge.

A central difficulty in liquid jet breakup is the accurate representation of nonlinear mode interactions. The interface does not evolve through isolated disturbances; instead, energy is transferred between different spatial modes through nonlinear geometric and inertial effects. These interactions determine whether disturbances decay, persist, or grow into large-amplitude oscillations leading to breakup. Therefore, a useful reduced-order framework must include nonlinear coupling terms between radius deformation modes and velocity modes rather than relying only on linearized descriptions.

In this work, we address this challenge by developing a nonlinear Galerkin reduced-order model to describe the dynamics of liquid jets.. Starting from the governing slender-jet equations, the interface radius and axial velocity fields are represented using finite modal expansions. The resulting equations are obtained through nondimensionalization and Galerkin projection, producing a six-state nonlinear dynamical system consisting of three radius modes and three velocity modes. The formulation retains the nonlinear coupling between interface deformation, capillary restoring forces, viscous dissipation, and modal energy exchange. This provides a compact yet physically meaningful representation of the dominant mechanisms controlling liquid jet evolution.

The objective of this study is to establish a reduced-order dynamical framework that captures the nonlinear behavior of liquid jets while avoiding the computational limitations of fully resolved free-surface simulations. The developed model is designed to capture the evolution of the dominant deformation modes, the interaction between the interface and the velocity fields, and the dynamic response of the jet as operating conditions vary. By transforming the breakup problem into a low-dimensional nonlinear system, the model enables detailed analysis of the mechanisms responsible for the transition from stable jet behavior to oscillatory and unstable regimes.

An additional advantage of the proposed reduced-order framework is its suitability for integration with advanced computational approaches. Because the model consists of a small number of coupled nonlinear ordinary differential equations, it provides an efficient platform for parameter exploration, stability characterization, and future development of physics-informed strategies for manipulating jet

© STM Journals 2026. All Rights Reserved 

behavior. Such a framework is particularly valuable for applications where controlling breakup characteristics, suppressing undesirable satellite droplets, or maintaining desired droplet distributions is required.

The novelty of this work lies in the development of a physics-based nonlinear Galerkin reduced-order model that bridges the gap between classical liquid jet theory and modern computational approaches for complex free-surface flows. Rather than treating breakup solely as a spatially resolved interface phenomenon, the proposed approach represents the jet as a nonlinear dynamical system governed by interacting modal structures. This perspective provides new insight into the mechanisms controlling liquid jet evolution and establishes a computationally efficient foundation for future studies involving nonlinear stability analysis and active manipulation of jet breakup dynamics.

## LITERATURE REVIEW

Papageorgiou [1] developed a theoretical framework for liquid-jet breakup by constructing analytical descriptions of pinch-off dynamics for viscous and inviscid jets and demonstrated that universal similarity solutions govern the final stages of capillary-driven singularity formation. Papageorgiou [2] subsequently developed a one-dimensional slender-jet model derived from the governing Stokes and Navier–Stokes equations and showed that the reduced formulation accurately captures nonlinear thread thinning, finite-time breakup, and satellite droplet formation while retaining the essential physics of the full free-surface problem. Ashgriz and Mashayek [3] investigated the temporal evolution of capillary jet instability and characterized the nonlinear growth of disturbances leading to jet disintegration and droplet formation, establishing important connections between instability development and breakup morphology. Teng *et al*. [4] developed predictive relationships for droplet size generated from cylindrical liquid jets and demonstrated the dependence of droplet characteristics on the governing flow parameters controlling jet breakup.

Richards *et al*. [5] examined drop formation in liquid–liquid jetting systems and showed that the competition among viscous forces, interfacial stresses, and inertia determines the transition between stable jetting and droplet formation regimes. Eggers and Dupont [6] introduced a one-dimensional approximation of the Navier–Stokes equations for free-surface flows and demonstrated that slender-jet formulations provide an efficient representation of droplet formation and capillary breakup while retaining the dominant nonlinear mechanisms of the full equations. Eggers [7] subsequently presented a comprehensive theoretical treatment of nonlinear free-surface dynamics and established a unified framework for describing pinch-off singularities, self-similar scaling, and universal features associated with liquid-jet breakup. Basaran [8] reviewed microscale free-surface flows with breakup and emphasized the importance of capillary instability, droplet formation, and breakup mechanisms in emerging applications such as microfluidics and printing technologies.

López-Herrera and Gañán-Calvo [9] investigated electrically influenced capillary-jet breakup and validated a reduced one-dimensional viscous-jet model against experimental observations, demonstrating the applicability of slender-jet descriptions to electrically driven and otherwise complex jet configurations. Notz and Basaran [10] studied the dynamics and breakup of contracting liquid filaments and demonstrated how viscosity and surface tension govern filament thinning, pinch-off, and the formation of satellite droplets. Eggers *et al*. [11] analyzed singular free-surface collapse phenomena and developed theoretical descriptions of nonlinear interface evolution associated with rapidly increasing curvature and capillary forces. van Hoeve W [12] provided a comprehensive review of the physics of liquid jets, including instability development, jet breakup, atomization, and droplet generation, thereby establishing a broad physical framework for understanding liquid fragmentation.

Van Hoeve *et al*. [13] experimentally investigated the breakup of diminutive Rayleigh jets and quantified the relationship among capillary instability, breakup wavelength, and resulting droplet characteristics at micron scales. Castrejón-Pita *et al*. [14] examined the breakup of liquid filaments and

© STM Journals 2026. All Rights Reserved 

identified the mechanisms governing neck evolution, pinch-off, and satellite-droplet generation during capillary-driven fragmentation. McIlroy and Harlen [15] developed numerical models for the breakup of particulate-suspension filaments and demonstrated that dispersed particles can significantly modify thinning dynamics and influence the resulting droplet morphology. Castrejón-Pita *et al*. [16] reviewed advances in inkjet technology and emphasized the importance of jet stability, suppression of satellite droplets, and precise control of breakup dynamics for industrial printing applications.

Hoath [17] provided a detailed treatment of droplet-generation mechanisms in inkjet systems and discussed the roles of capillary waves, ligament formation, satellite droplets, and fluid properties in determining printing performance. Wang *et al*. [18] investigated liquid-jet breakup using numerical simulations and analyzed the mechanisms responsible for primary, satellite, and subsatellite droplet formation during nonlinear jet evolution. Castrejón-Pita *et al*. [19] synthesized developments in liquid-jet breakup research and emphasized the integration of theoretical modeling, computational simulations, and experimental diagnostics for understanding complex droplet-formation processes. Driessen *et al*. [20] investigated the stability of inkjet-generated droplets and demonstrated how operating conditions influence breakup dynamics, droplet uniformity, and satellite-droplet production.

Soni *et al*. [21] studied droplet deformation and breakup under aerodynamic forcing and demonstrated that the interaction among inertial, viscous, and surface-tension forces determines the resulting fragmentation behavior. Ade *et al*. [22] experimentally characterized droplet-size distributions during atomization using high-resolution imaging and established relationships between breakup mechanisms and the resulting droplet statistics. Ade, Chandrala, and Sahu [23] further investigated the breakup of individual droplets at moderate Weber numbers and demonstrated that the balance between inertial and capillary forces strongly influences secondary breakup and droplet-size distribution. Srinivasan and Sinha [24] examined the influence of jet velocity profiles on primary liquid-jet breakup and demonstrated that nozzle-exit conditions can strongly affect instability growth, breakup length, and the resulting droplet characteristics. Wang *et al*. [25] developed a thermodynamic interpretation of liquid-jet breakup and connected energy evolution, interfacial dynamics, and droplet-formation mechanisms to provide additional insight into nonlinear fragmentation processes.

Overall, the literature demonstrates a progressive development from fundamental analytical descriptions of capillary pinch-off and similarity solutions toward reduced-order slender-jet models, numerical simulations, experimental characterization, and application-oriented studies of droplet formation. Early investigations by Papageorgiou [1, 2], Ashgriz and Mashayek [3], Eggers and Dupont [6], and Eggers [7] established the fundamental instability and singularity mechanisms governing liquid-jet breakup. Subsequent studies by López-Herrera and Gañán-Calvo [9], Notz and Basaran [10], and McIlroy and Harlen [15] demonstrated the importance of reduced-dimensional modeling and the influence of complex physical effects on filament thinning and pinch-off. More recent investigations have increasingly focused on inkjet printing, droplet stability, aerodynamic forcing, droplet-size distributions, nonuniform velocity profiles, and thermodynamic effects [16–25].

These developments provide a strong foundation for further reduced-order and nonlinear-dynamical modeling of liquid-jet breakup, particularly approaches that can combine bifurcation analysis, stability characterization, and computationally efficient representations of the underlying multiphase dynamics.

This body of work establishes that liquid-jet breakup is governed by the nonlinear interaction between capillary forces, inertia, viscosity, and interface deformation. However, most existing studies focus on direct numerical simulation, asymptotic analysis, or experimental characterization of breakup dynamics. A reduced-order dynamical framework capable of representing the dominant instability modes, capturing nonlinear mode interactions, and providing a computationally efficient platform for stability analysis and active manipulation of jet breakup remains a potentially valuable research direction. This motivates the development of the present Galerkin-based reduced-order model for liquid-jet dynamics [26-27].

© STM Journals 2026. All Rights Reserved 

**Objectives and Novelty of the Present Study**

The primary objective of this study is to develop a physics-based reduced-order framework to predict, analyze, and control the nonlinear dynamics of liquid jet breakup and satellite droplet formation. While the capillary instability of liquid jets has been extensively studied through linear stability theory and direct numerical simulations, the transition from small-amplitude disturbances to finite-amplitude nonlinear oscillations remains challenging due to the strongly coupled effects of inertia, surface tension, viscous dissipation, and nonlinear interface deformation. The present work addresses this challenge by constructing a low-dimensional nonlinear dynamical model that retains the dominant physical mechanisms governing jet instability while enabling efficient bifurcation analysis and optimal control.

The first objective is to derive a nonlinear Galerkin-based reduced-order model from the governing free-surface dynamics of an axisymmetric liquid jet. The model represents the interface deformation and associated velocity field using a finite number of dominant spatial modes, resulting in a six-state nonlinear ordinary differential equation system. Unlike purely linear stability models, the proposed ROM incorporates nonlinear modal interactions that govern energy transfer between deformation modes, enabling prediction of finite-amplitude oscillatory states beyond the instability threshold. The resulting model provides a computationally efficient representation of the jet dynamics while preserving the essential physics of capillary-driven breakup.

The second objective is to characterize the nonlinear stability landscape of the reduced-order system through dynamical systems analysis. The Weber number is selected as the primary bifurcation parameter because it directly controls the competition between inertial and capillary forces. By performing equilibrium continuation and eigenvalue analysis, the evolution of the steady jet state is tracked as the Weber number varies. The identification of Hopf bifurcation points provides quantitative information on the transition from stable steady operation to self-sustained oscillatory dynamics associated with nonlinear jet deformation and the onset of breakup.

The third objective is to analyze the nonlinear oscillations emerging after instability using limit-cycle continuation. The resulting periodic solutions provide insight into the amplitude saturation, oscillation frequency, and modal interactions associated with finite-amplitude jet disturbances. The ability of the reduced-order model to capture stable limit cycles following a supercritical Hopf bifurcation establishes a direct connection between instability theory and the nonlinear dynamics underlying periodic necking and satellite droplet generation.

The fourth objective is to formulate an optimal control framework in which the Weber number is actively manipulated to regulate the jet dynamics. Since the Weber number can be physically modified through changes in jet velocity, inlet pressure, or flow-rate control, it provides a realistic actuation mechanism for suppressing unwanted oscillations or maintaining the jet near a desired operating state. The optimization problem minimizes deviations of the modal amplitudes from a target configuration while penalizing excessive control effort, thereby identifying the minimum physical intervention required to stabilize the nonlinear jet dynamics.

The final objective is to establish a foundation for data-driven stability prediction by generating a bifurcation-informed dataset from the reduced-order model. The equilibrium states, Weber number values, and associated eigenvalue information provide a physics-based database that can be used to construct surrogate models capable of rapidly predicting stability boundaries and critical operating conditions. This combination of nonlinear dynamics, reduced-order modeling, and data-driven analysis provides a pathway toward efficient real-time prediction and control of liquid jet breakup processes.

The main contribution of this work is the combination of nonlinear Galerkin reduced-order modeling with Hopf bifurcation analysis, limit-cycle characterization, and optimal Weber-number control to study liquid jet breakup within a single framework. Previous studies have primarily focused either on

© STM Journals 2026. All Rights Reserved 

linear instability mechanisms, high-fidelity numerical simulations, or passive characterization of breakup behavior. In contrast, the present approach develops a low-dimensional dynamical model that not only identifies the transition to oscillatory instability but also enables active manipulation of the instability through a physically meaningful control parameter. By connecting fundamental capillary instability physics with bifurcation-aware optimal control, this work provides a new framework for understanding, predicting, and regulating nonlinear jet breakup and satellite droplet formation. The remainder of this paper is organized as follows. The governing model equations are presented first, followed by a description of the numerical methods. The results are then discussed, and the paper concludes with a summary of the main findings.

**Reduced-Order Galerkin Model for Liquid Jet Breakup Dynamics**

The breakup of a liquid jet is governed by a complex interplay between inertial, capillary, viscous, and nonlinear convective effects. Although the full three-dimensional Navier–Stokes equations provide a complete description of the flow, the prediction of instability onset, nonlinear oscillations, and satellite droplet formation requires resolving a wide range of spatial and temporal scales. This multiscale nature makes direct numerical simulation computationally expensive, particularly when repeated simulations are required for stability analysis, bifurcation tracking, or active control design. A reduced-order representation that retains the dominant physical mechanisms while significantly reducing computational complexity is therefore essential.

The present work develops a nonlinear Galerkin-based reduced-order model (ROM) for the dynamics of an axisymmetric liquid jet undergoing capillary-driven breakup. The central idea is to represent the evolving jet interface as a finite-dimensional combination of spatial deformation modes, where the modal amplitudes describe the temporal evolution of the dominant instability structures. This approach is motivated by the observation that near the onset of breakup, the dynamics are often dominated by a small number of coherent modes associated with the growth, interaction, and saturation of interfacial disturbances. Consequently, the infinite-dimensional free-surface evolution problem can be projected onto a low-dimensional nonlinear dynamical system while preserving the essential mechanisms responsible for instability development.

The jet radius is decomposed into a base cylindrical state and a perturbation field. The perturbation is expanded using a Galerkin representation containing three dominant interface deformation modes. The associated modal velocity amplitudes are introduced through the kinematic evolution of the interface, resulting in a six-dimensional state space consisting of three radius modes and three velocity modes. Projection of the governing free-surface equations onto the selected basis functions produces a set of coupled nonlinear ordinary differential equations. The linear contributions describe the natural oscillatory response and viscous attenuation of the individual modes, while the nonlinear terms represent energy transfer between modes arising from geometric nonlinearities, convective effects, and capillary interactions.

The Weber number is selected as the principal bifurcation parameter because it directly quantifies the competition between inertial and surface-tension forces. Increasing the Weber number reduces the relative influence of capillary restoration and promotes larger interfacial deformations, thereby driving the system toward instability and eventual breakup. Within the reduced-order framework, the Weber number modifies the nonlinear restoring terms and controls the transition between stable steady jet configurations and oscillatory states. This allows the onset of instability to be characterized using classical dynamical-systems tools, including equilibrium continuation, eigenvalue analysis, and Hopf bifurcation theory.

An important feature of the present formulation is that the ROM preserves the nonlinear mechanisms required to capture finite-amplitude oscillatory behavior. Linear stability analysis alone can identify the initial growth of disturbances but cannot describe the nonlinear saturation that leads to periodic

© STM Journals 2026. All Rights Reserved 

oscillations or limit-cycle dynamics. The inclusion of nonlinear modal coupling enables the reduced model to reproduce the emergence of stable periodic solutions associated with nonlinear jet oscillations preceding satellite droplet formation. The resulting low-dimensional system therefore provides a bridge between fundamental instability theory and computationally efficient prediction of nonlinear breakup dynamics. The derived reduced-order model also provides a natural framework for active control. Since the Weber number can be experimentally modified through variations in jet velocity, flow rate, or inlet pressure, it serves not only as a bifurcation parameter but also as a physically realizable control variable. By embedding the Weber number as a time-dependent control input, the ROM enables optimization strategies aimed at suppressing undesirable oscillations, delaying breakup, or steering the jet toward a desired operating state. Thus, the Galerkin formulation provides a unified framework connecting the fundamental physics of capillary instability with bifurcation analysis and optimal control of liquid jet breakup.

Consider an incompressible Newtonian liquid jet with radius $h(z,t)$, axial velocity $w(z,r,t)$, density $\rho$, viscosity $\mu$, and surface tension $\sigma$. The governing dynamics are described by the incompressible Navier–Stokes equations

$$\nabla \cdot \mathbf{u} = 0$$
$$\rho\left(\frac{\partial \mathbf{u}}{\partial t} + \mathbf{u} \cdot \nabla \mathbf{u}\right) = -\nabla p + \mu \nabla^2 \mathbf{u} \tag{1}$$

For an axisymmetric jet, the velocity field is expressed as

$$\mathbf{u} = (u_r, w_z), \tag{2}$$

where $u_r$ and $w_z$ denote the radial and axial velocity components, respectively. The free-surface evolution is governed by the kinematic condition

$$\frac{\partial h}{\partial t} + w_z \frac{\partial h}{\partial z} = u_r \tag{3}$$

while the normal stress balance at the interface is

$$p - p_g = \sigma\kappa + 2\mu \frac{\partial u_r}{\partial r} \tag{4}$$

where the interface curvature is

$$\kappa = \frac{1}{h(1+h_z^2)^{1/2}} - \frac{h_{zz}}{\left(1+h_z^2\right)^{3/2}} \tag{5}$$

The equations are nondimensionalized using the characteristic jet radius $R_0$, velocity $U_0$, and time scale

$$t_c = \frac{R_0}{U_0} \tag{6}$$

The nondimensional variables are defined as

$$\hat{z} = \frac{z}{R_0}, \hat{t} = \frac{tU_0}{R_0}, \hat{h} = \frac{h}{R_0} \tag{7}$$

The dominant dimensionless parameter controlling the breakup dynamics is the Weber number

© STM Journals 2026. All Rights Reserved 

$$We = \frac{\rho U_0^2 R_0}{\sigma} \tag{8}$$

which represents the ratio between inertial and capillary forces. Therefore, the Weber number is selected as the bifurcation and control parameter

The interface deformation is represented as a perturbation from the cylindrical base state

$$h(z,t) = 1 + \eta(z,t) \tag{9}$$

where $\eta(z,t)$ represents the disturbance amplitude. The disturbance field is approximated using a Galerkin expansion:

$$\boxed{\eta(z,t) = a_1(t)\phi_1(z) + a_2(t)\phi_2(z) + a_3(t)\phi_3(z)} \tag{10}$$

where $a_1(t), a_2(t), a_3(t)$ are the time-dependent amplitudes of the dominant interface modes and $\phi_i(z)$ are the spatial basis functions. The corresponding interface velocity is expanded using the same modal basis:

$$\frac{\partial \eta}{\partial t} = b_1(t)\phi_1(z) + b_2(t)\phi_2(z) + b_3(t)\phi_3(z) \tag{11}$$

which gives the kinematic relations

$$\frac{da_1}{dt} = b_1, \frac{da_2}{dt} = b_2, \frac{da_3}{dt} = b_3 \tag{12}$$

Substitution of the Galerkin representation into the governing equations and projection onto each spatial basis function using

$$< R, \phi_i >= 0 \tag{13}$$

produces a finite-dimensional nonlinear dynamical system. The first three equations describe the evolution of the interface deformation modes. Linear damping terms represent viscous dissipation, while nonlinear terms describe modal interactions arising from the convective and capillary nonlinearities.

The resulting radius-mode equations are:

$$\begin{aligned}
\frac{da_1}{dt} &= b_1 - \alpha_1 a_1 + \beta_1 a_1 a_2 \\
\frac{da_2}{dt} &= b_2 - \alpha_2 a_2 + \beta_2 a_1^2 + \gamma_2 a_1 a_3 \\
\frac{da_3}{dt} &= b_3 - \alpha_3 a_3 + \beta_3 a_1 a_2
\end{aligned} \tag{14}$$

The momentum projection generates second-order modal oscillator equations. These equations contain inertial, viscous, capillary, and nonlinear coupling contributions. The capillary restoring force scales with $1/We$, reflecting the competition between inertia and surface tension.

The first velocity mode equation is:

© STM Journals 2026. All Rights Reserved 

$$\frac{db_1}{dt} = -\omega_1^2 a_1 - \zeta_1 b_1 + \frac{1}{We}\left(a_1 - a_1^3\right) + \eta_1 a_2 b_1 + F \tag{15}$$

The second velocity mode equation is:

$$\frac{db_2}{dt} = -\omega_2^2 a_2 - \zeta_2 b_2 + \frac{1}{We}\left(a_2 - a_1^2\right) + \eta_2 a_1 b_2 \tag{16}$$

The third velocity mode equation is:

$$\frac{db_3}{dt} = -\omega_3^2 a_3 - \zeta_3 b_3 + \frac{1}{We}\left(a_3 - a_1 a_2\right) + \eta_3 a_2 b_3 \tag{17}$$

The final ODE set is

$$\begin{aligned}
\frac{da_1}{dt} &= b_1 - \alpha_1 a_1 + \beta_1 a_1 a_2 \\
\frac{da_2}{dt} &= b_2 - \alpha_2 a_2 + \beta_2 a_1^2 + \gamma_2 a_1 a_3 \\
\frac{da_3}{dt} &= b_3 - \alpha_3 a_3 + \beta_3 a_1 a_2 \\
\frac{db_1}{dt} &= -\omega_1^2 a_1 - \zeta_1 b_1 + \frac{1}{We}\left(a_1 - a_1^3\right) + \eta_1 a_2 b_1 + F \\
\frac{db_2}{dt} &= -\omega_2^2 a_2 - \zeta_2 b_2 + \frac{1}{We}\left(a_2 - a_1^2\right) + \eta_2 a_1 b_2 \\
\frac{db_3}{dt} &= -\omega_3^2 a_3 - \zeta_3 b_3 + \frac{1}{We}\left(a_3 - a_1 a_2\right) + \eta_3 a_2 b_3
\end{aligned} \tag{18}$$

Tables 1 and 2 summarize the variable and parameter details

**Table 1.** State Variables and Control Variable of the Six-State Liquid Jet Reduced-Order Model

| Symbol | Description | Units |
|---|---|---|
| $a_1$ | First Galerkin mode amplitude representing the dominant jet radius deformation | Dimensionless |
| $a_2$ | Second Galerkin mode amplitude representing higher-order radius deformation | Dimensionless |
| $a_3$ | Third Galerkin mode amplitude representing higher-order radius deformation | Dimensionless |
| $b_1$ | First Galerkin mode velocity amplitude associated with $a_1$ | Dimensionless time $^{-1}$ |
| $b_2$ | Second Galerkin mode velocity amplitude associated with $a_2$ | Dimensionless time $^{-1}$ |
| $b_3$ | Third Galerkin mode velocity amplitude associated with $a_3$ | Dimensionless time $^{-1}$ |
| $x$ | Reduced-order state vector, $x = [a_1, a_2, a_3, b_1, b_2, b_3]^T$ | Dimensionless |
| $t$ | Nondimensional time variable | $R_0 / U_0$ |
| $We$ | Weber number, $We = \rho U_0^2 R_0 / \sigma$ , used as bifurcation parameter and control variable | Dimensionless |

© STM Journals 2026. All Rights Reserved 

| Symbol | Description | Units |
|---|---|---|
| $u(t)$ | Optimal control input modifying the Weber number, $We(t) = We_0 + u(t)$ | Dimensionless |
| $\eta(z,t)$ | Dimensionless jet interface disturbance | Dimensionless |
| $\phi_i(z)$ | Galerkin spatial basis functions for interface deformation modes | Dimensionless |
| $R_0$ | Characteristic jet radius | m |
| $U_0$ | Characteristic jet exit velocity | m/s |
| $\rho$ | Liquid density | kg/m$^3$ |
| $\mu$ | Dynamic viscosity | Pa·s |
| $\sigma$ | Surface tension coefficient | N/m |

**Table 2.** Model Parameters of the Six-State Liquid Jet Reduced-Order Model

| Symbol | Description | Value | Units |
|---|---|---|---|
| $\omega_1$ | Natural frequency of first Galerkin mode | 1.0 | Dimensionless |
| $\omega_2$ | Natural frequency of second Galerkin mode | 2.0 | Dimensionless |
| $\omega_3$ | Natural frequency of third Galerkin mode | 5.0 | Dimensionless |
| $\zeta_1$ | Linear damping coefficient of first velocity mode | 0.05 | Dimensionless |
| $\zeta_2$ | Linear damping coefficient of second velocity mode | 0.08 | Dimensionless |
| $\zeta_3$ | Linear damping coefficient of third velocity mode | 0.10 | Dimensionless |
| $\alpha_1$ | Linear damping coefficient for first radius mode | 0.50 | Dimensionless |
| $\alpha_2$ | Linear damping coefficient for second radius mode | 0.15 | Dimensionless |
| $\alpha_3$ | Linear damping coefficient for third radius mode | 0.15 | Dimensionless |
| $\beta_1$ | Nonlinear coupling coefficient between $a_1$ and $a_2$ | 0.50 | Dimensionless |
| $\beta_2$ | Quadratic self-interaction coefficient of first radius mode | 0.50 | Dimensionless |
| $\beta_3$ | Nonlinear coupling coefficient between $a_1$ and $a_2$ for third mode | 1.00 | Dimensionless |
| $\gamma_2$ | Cross-mode coupling coefficient between $a_1$ and $a_3$ | 0.50 | Dimensionless |
| $\eta_1$ | Nonlinear radius–velocity coupling coefficient for first mode | 0.50 | Dimensionless |
| $\eta_2$ | Nonlinear radius–velocity coupling coefficient for second mode | 0.50 | Dimensionless |
| $\eta_3$ | Nonlinear radius–velocity coupling coefficient for third mode | 0.50 | Dimensionless |
| $F$ | External forcing/base-flow contribution | 0.50 | Dimensionless |
| $We_H$ | Critical Weber number at Hopf bifurcation | 0.251008 | Dimensionless |
| $L_1$ | First Lyapunov coefficient at Hopf point | $-1.110962\times10^{-2}$ | Dimensionless |
| $\omega_H$ | Hopf oscillation frequency | 0.3671 | Dimensionless time$^{-1}$ |

© STM Journals 2026. All Rights Reserved 

**Bifurcation Analysis and Optimal Control**

The MATLAB software MATCONT (Dhooge *et al* 2003 ) [26] was used to perform the bifurcation analysis. Pyomo. DAE ( a Python software was used in conjunction with IPOPT .

**Formation of Stability Dataset from MATCONT Results**

A stability dataset was generated from numerical continuation calculations performed in MATCONT. Each row in the dataset corresponds to an equilibrium point along the continuation branch and contains the state variables, the bifurcation parameter, and a measure of the system's stability.

At each equilibrium point, the Jacobian matrix was evaluated numerically, and its eigenvalues were calculated in MATLAB. The largest real part of these eigenvalues was then used as a scalar measure of stability. In MATLAB, this quantity was calculated as eig_real_max = max(real(eigvals)).

This measure provides a simple way to determine the local stability of each equilibrium point. Negative values indicate locally asymptotically stable equilibria, whereas positive values indicate unstable equilibria. A change in sign through zero provides an indication of a stability transition associated with a Hopf bifurcation when the corresponding critical eigenvalues form a complex-conjugate pair.

The resulting stability dataset was saved as a CSV file and can be used for subsequent regression or classification analyses to identify stability boundaries and estimate the locations of bifurcation points.

**Neural Network Surrogate for Stability Prediction**

Directly incorporating eigenvalue calculations into IPOPT-based optimal control is not practical for several reasons. Eigenvalues would need to be calculated at every collocation point, which can be computationally demanding. In addition, the required repeated evaluation of the Jacobian matrix further increases the computational cost. Finally, incorporating eigenvalue calculations into the symbolic differentiation required for large-scale nonlinear programming is challenging.

Before neural-network training, we standardized all input variables to improve numerical conditioning and training stability. Let $x_{\text{raw}}$ denote the vector of state variables and bifurcation parameters obtained from the stability dataset. For every input variable $j$, the training mean $\mu_j$ and training standard deviation $\sigma_j$ were computed over all training samples. The standardized inputs were defined as

$$x_j = \frac{x_{\text{raw},j} - \mu_j}{\max\left(\sigma_j, \varepsilon_{\text{scale}}\right)} \tag{19}$$

where $\varepsilon_{\text{scale}}$ is a small positive regularization parameter introduced to prevent numerical singularities associated with extremely small variances.

All inputs are scaled while avoiding excessively large neural-network activation arguments during optimization. The procedure enhances the robustness of gradient-based optimization. The vectors $\mu$ and $\sigma$ computed during training were stored and embedded identically within the Pyomo optimal-control formulation to ensure consistency between neural-network training and deployment.

To eliminate the need for repeated eigenvalue calculations during optimization, a feedforward neural network is trained to predict the maximum real part of the eigenvalues from the system states and the bifurcation parameter. Hyperbolic tangent activation functions are used to provide the smooth differentiability needed for integration with the IPOPT optimization framework.

© STM Journals 2026. All Rights Reserved 

If the input vector is denoted by $x$, representing the scaled variables, the network architecture is defined as

$$\hat{\lambda}_{\max} = f_{\mathrm{NN}}(x) \tag{20}$$

where $W_i$ and $b_i$ denote the weight matrices and bias vectors of the neural network. The hidden-layer variables $z_1$ and $z_2$ represent nonlinear transformations of the input variables and intermediate features. The final output $\hat{\lambda}_{\max}$ provides a smooth approximation of the spectral abscissa. The hyperbolic tangent activation function is smooth and continuously differentiable, allowing the neural-network surrogate to provide the first- and second-order derivatives needed by IPOPT. Bias terms are also included in the network to improve its flexibility, since omitting them would unnecessarily restrict the range of functions that the network can represent.

$f_{\mathrm{NN}}(\cdot)$ represents the nonlinear input–output mapping learned by the neural network, and approximates the relationship between the scaled system variables and the spectral abscissa $\lambda_{\max}$.

$z_1$ and $z_2$ represent nonlinear combinations of the inputs and previously extracted features. Every component of $z_1$ forms a smooth nonlinear combination of the original variables, while each component of $z_2$ captures higher-level nonlinear features derived from $z_1$. The final network output $\hat{\lambda}_{\max}$ acts as a differentiable approximation of the maximum real eigenvalue, enabling efficient stability evaluation during optimization.

**Stability-Penalized Optimal Control Formulation**

The neural-network prediction is included directly in the objective function as a quadratic stability penalty. Instead of enforcing stability through a strict constraint, the optimization penalizes deviations of the predicted spectral abscissa from zero, allowing stability considerations to be incorporated smoothly into the optimization process.

The modified objective function is given by $\sum optv(t) + \alpha_{Hopf} \sum_{k=1}^{N} \hat{\lambda}_{\max,k}^{2}$, where $\sum optv(t)$ denotes the original optimal-control objective function, $\hat{\lambda}_{\max,k}$ is the neural-network prediction of the maximum real eigenvalue at collocation point $k$, and $\alpha_{Hopf}$ is a weighting parameter controlling the importance of stability in the optimization process. The quadratic penalty encourages the predicted spectral abscissa to remain close to zero. In this way, the optimized trajectories are guided toward the stability boundary while discouraging solutions with large positive or negative spectral-abscissa values.

Increasing $\alpha_{Hopf}$ places greater emphasis on stability preservation, whereas setting $\alpha_{Hopf} = 0$ removes the stability penalty entirely and recovers the original optimal-control problem. This formulation is smooth and differentiable, making it well suited for gradient-based optimization with IPOPT. Using the neural-network surrogate also avoids repeated Jacobian evaluations and eigenvalue calculations during the optimization, which reduces the overall computational cost. In this way, stability information obtained from the bifurcation analysis can be included in the optimal-control problem without sacrificing computational efficiency or numerical robustness.

To integrate the neural network into the optimization framework, it is trained using the stability dataset obtained from the MATCONT continuation analysis. For each equilibrium point, the Jacobian matrix is evaluated and its eigenvalues are calculated. The spectral abscissa, defined as the largest real part of the eigenvalues, is then used as the stability metric.

© STM Journals 2026. All Rights Reserved 

$$\lambda_{\max} = \max \Re\left(\lambda\left(J\right)\right) \tag{21}$$

Negative values of the spectral abscissa correspond to stable equilibria, while positive values indicate instability. A zero crossing associated with a complex-conjugate pair of eigenvalues indicates a Hopf bifurcation. Here, $J$denotes the Jacobian matrix of the steady-state ODE system. The resulting neural-network surrogate provides an efficient and differentiable approximation of this stability measure, allowing stability to be incorporated into the optimal-control problem without explicitly calculating eigenvalues during the optimization.

**RESULTS**

A Hopf bifurcation point was found at $(a_1, a_2, a_3, b_1, b_2, b_3, we)$ values of ( 0.141286 -4.546652 0.048410 0.391832 -0.695398 0.649639 0.251008) . The first Lyapunov coefficient is -1.110962e-02. The limit cycle for this Hopf bifurcation point is shown in Fig. 1.

The analytical expression for the Jacobian matrix is

$$J_a = \begin{bmatrix} -\alpha_1 + \beta_1 a_2 & \beta_1 a_1 & 0 & 1 & 0 & 0 \\ 2\beta_2 a_1 + \gamma_2 a_3 & -\alpha_2 & \gamma_2 a_1 & 0 & 1 & 0 \\ \beta_3 a_2 & \beta_3 a_1 & -\alpha_3 & 0 & 0 & 1 \\ -\omega_1^2 + \dfrac{1-3a_1^2}{We} & \eta_1 b_1 & 0 & -\zeta_1 + \eta_1 a_2 & 0 & 0 \\ -\dfrac{2a_1}{We} + \eta_2 b_2 & -\omega_2^2 + \dfrac{1}{We} & 0 & 0 & -\zeta_2 + \eta_2 a_1 & 0 \\ -\dfrac{a_2}{We} & -\dfrac{a_1}{We} + \eta_3 b_3 & -\omega_3^2 + \dfrac{1}{We} & 0 & \eta_3 a_2 & -\zeta_3 + \eta_3 a_2 \end{bmatrix} \tag{22}$$

The numerical Jacobian matrix at the Hopf Bifurcation point is

$$J_n = \begin{bmatrix} -2.773326 & 0.070643 & 0 & 1 & 0 & 0 \\ 0.165491 & -0.150000 & 0.070643 & 0 & 1 & 0 \\ -4.546652 & 0.141286 & -0.150000 & 0 & 0 & 1 \\ 2.745358 & 0.195916 & 0 & -2.323326 & 0 & 0 \\ -1.473448 & -0.016063 & 0 & 0 & -0.009357 & 0 \\ 18.113574 & -0.238055 & -21.016063 & 0 & -2.273326 & -2.373326 \end{bmatrix} \tag{23}$$

The eigenvalues of this matrix are 0.367099i , -0.367099i, −4.217801, −1.038536, −1.261048+4.446494i, −1.261048-4.446494i. The presence of 2 imaginary Hopf bifurcation points of opposite sign confirms the existence of the Hopf Bifurcation .

The optimal control minimizes the function

$$\begin{aligned} &\sum optv(t) = \sum (a_1(t) - a_1^*)^2 + (a_2(t) - a_2^*)^2 + (a_3(t) - a_3^*)^2 + \\ &(b_1(t) - b_1^*)^2 + (b_2(t) - b_2^*)^2 + b_3(t) - b_3^*)^2 + (u(t))^2 \\ &u(t) = we(t) - 0.3; \\ &a_1^* = 0.141286; a_2^* = -4.546652 a_3^* = 0.048410; \\ &b_1^* = 0.391832; b_2^* = -0.695398; b_3^* = 0.649639. \end{aligned} \tag{24}$$

© STM Journals 2026. All Rights Reserved 

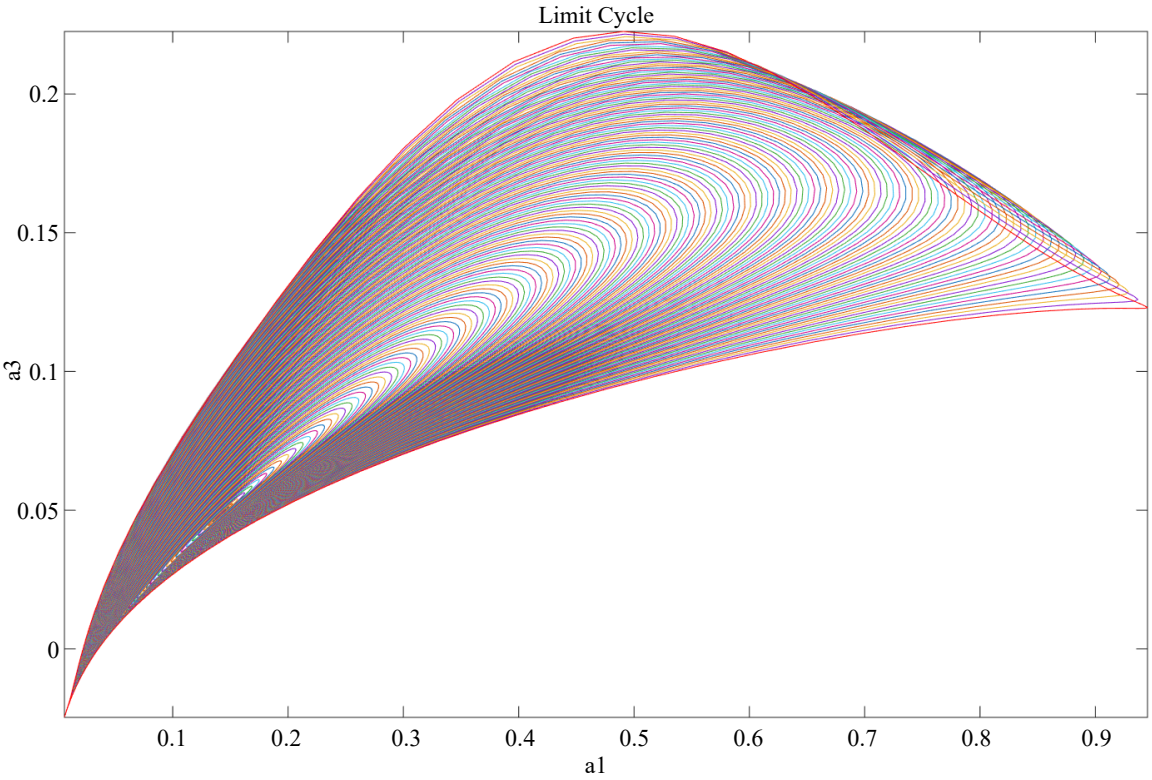



**Figure 1.** Limit Cycle Caused by Hopf Bifurcation

without and with the constraint imposed by the Hopf bifurcation . The optimization objective drives the reduced-order dynamics toward a desired steady jet configuration by minimizing the deviations of the Galerkin modal amplitudes from their target values while penalizing excessive control action. Physically, this corresponds to suppressing the nonlinear oscillations responsible for necking and the onset of satellite-droplet formation, while maintaining the smallest possible modulation of the Weber number. Because the control variable is the Weber number, the optimization identifies the minimum time-varying adjustment of the Weber number required to maintain the jet near the desired equilibrium, thereby delaying or suppressing the oscillatory dynamics that precede jet breakup. Physically, the Weber number can be manipulated by adjusting the jet exit velocity, modifying the nozzle diameter, changing the fluid surface tension via surfactants or temperature control, or altering the fluid density, thereby shifting the balance between inertial and capillary forces that govern jet stability.

Without a Hopf constraint , $\alpha_{Hopf}$ =0, $\sum(optv(t)+\alpha_{hopf}.s_{\max}(\lambda+\varepsilon_1))^2$ the obtained value of $\sum optv(t)$ was 6.843. For a Hopf constraint, $\alpha_{Hopf}=100$ , the obtained value of $\sum optv(t)$ was 3.33.

This shows a considerable decrease in the minimized function, indicating the effect of the Hopf bifurcation constraint. This corresponds to a 49 % reduction in the minimized objective function value. Figs 2a, 2b, and 2c show the optimal control profiles without the Hopf constraint, and Figs 3a, 3b, and 3c show the optimal control profiles with the Hopf constraint.

## DISCUSSION

The present results demonstrate that a low-dimensional nonlinear reduced-order model can capture the essential dynamical features of liquid jet instability, including the transition from steady to oscillatory behavior and the subsequent regulation of these instabilities through active control. The central outcome of this study is the identification and characterization of a Hopf bifurcation in a

© STM Journals 2026. All Rights Reserved 

Galerkin-based six-state representation of the liquid jet dynamics. This result is significant because it establishes a direct connection between the nonlinear modal interactions governing interface deformation and the emergence of finite-amplitude oscillations that precede breakup and satellite droplet formation. Unlike linear stability approaches, which primarily describe the initial exponential amplification of disturbances, the present formulation provides access to the nonlinear evolution of the instability beyond the critical point.

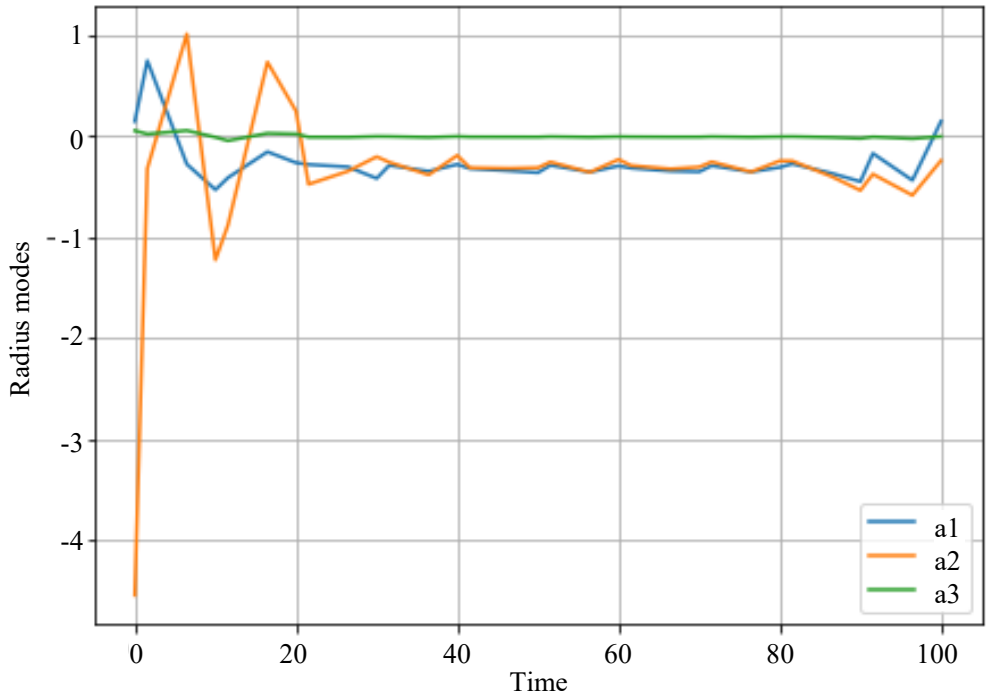



**Figure 2a.** Radius Nodes without Hopf control.

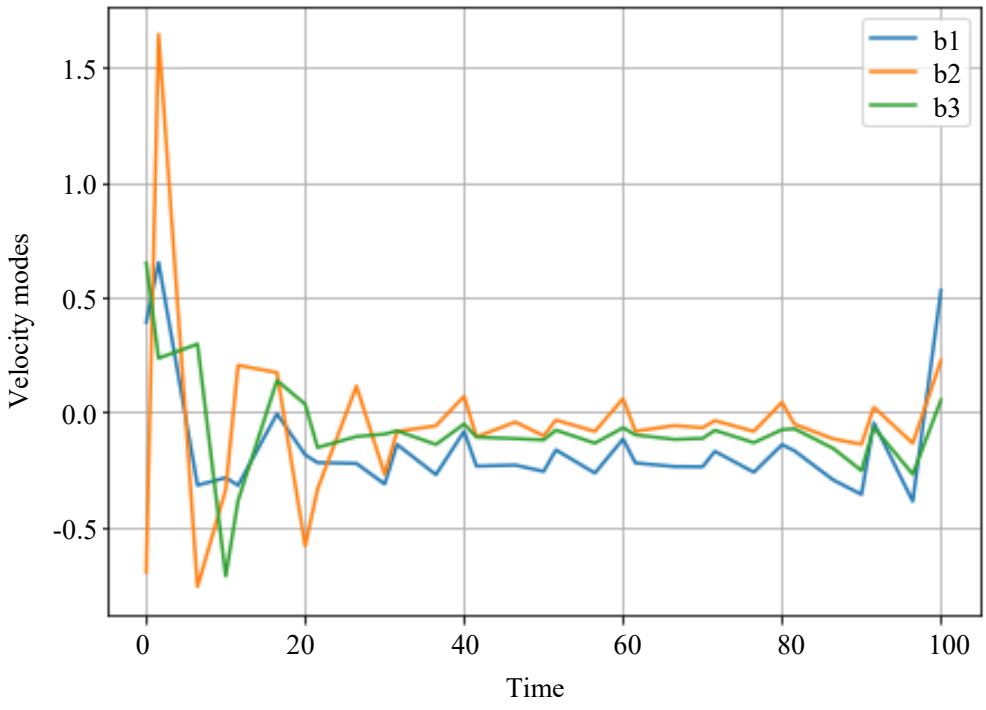



**Figure 2b.** Velocity Nodes without Hopf control.

© STM Journals 2026. All Rights Reserved 

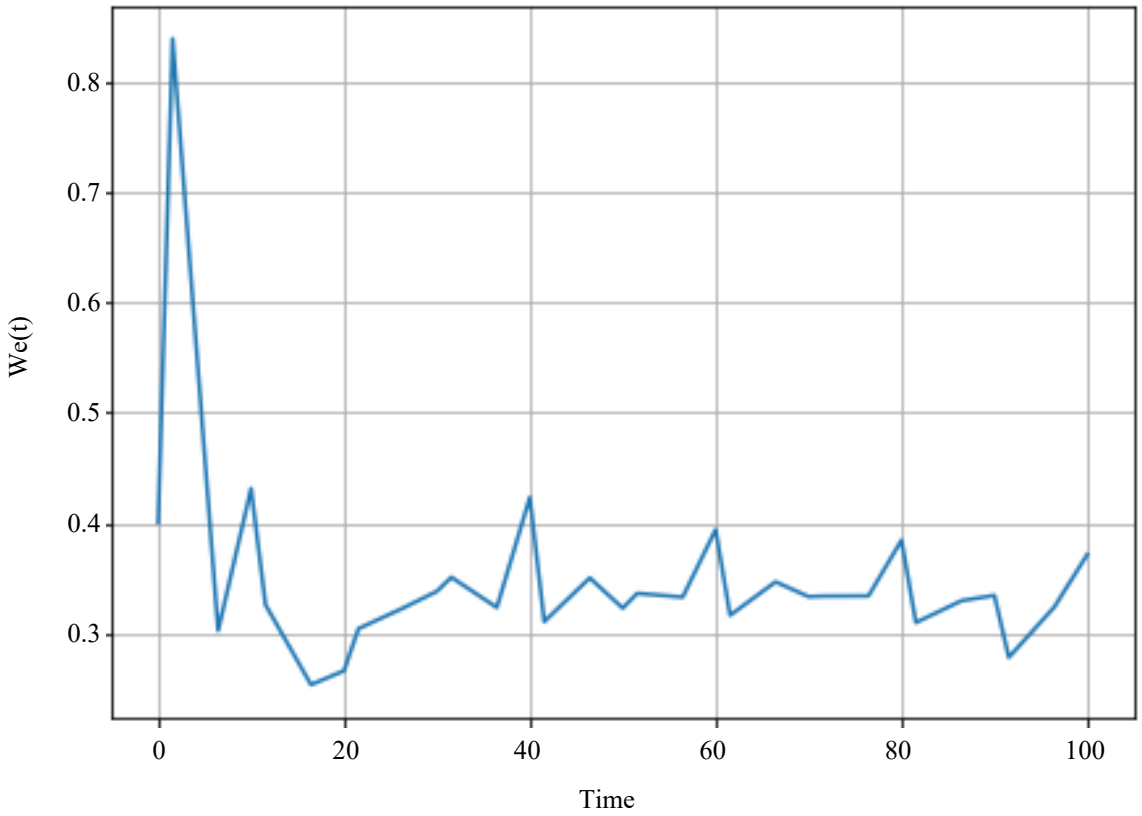



**Figure 2c.** Control profile without Hopf control.

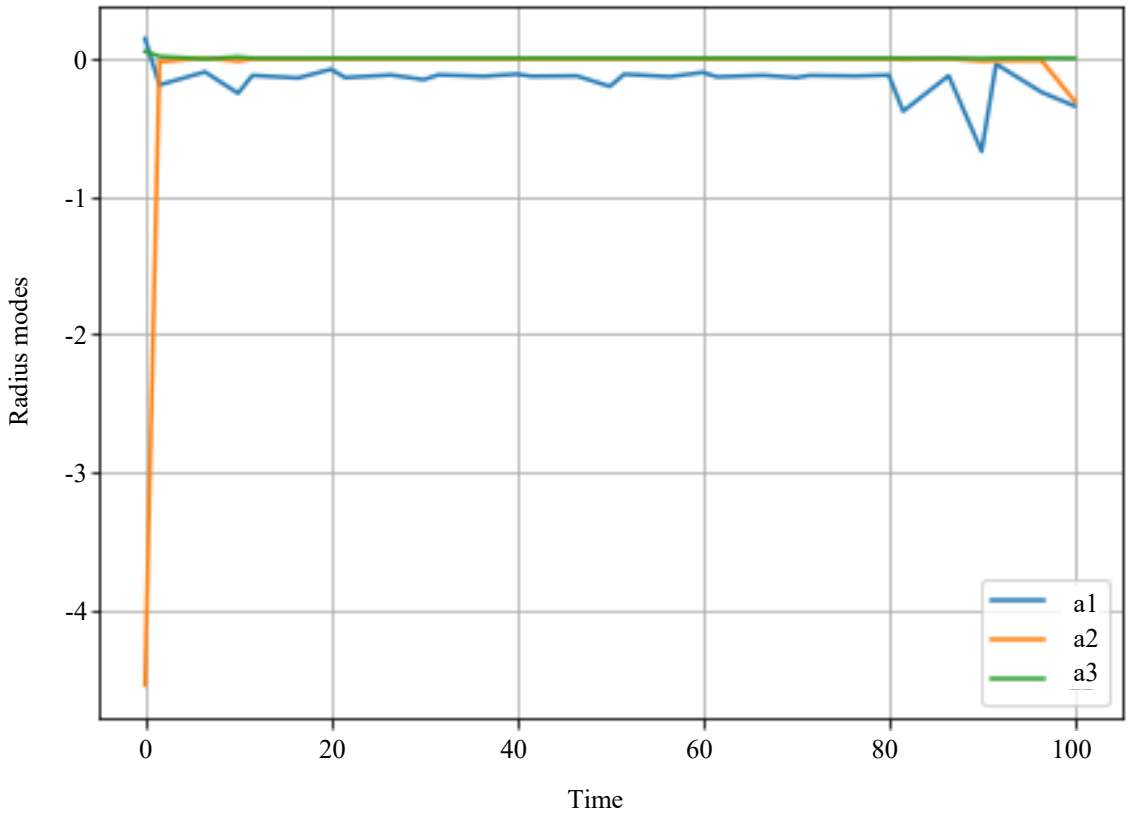



**Figure 3a.** Radius Nodes with Hopf control.

© STM Journals 2026. All Rights Reserved 

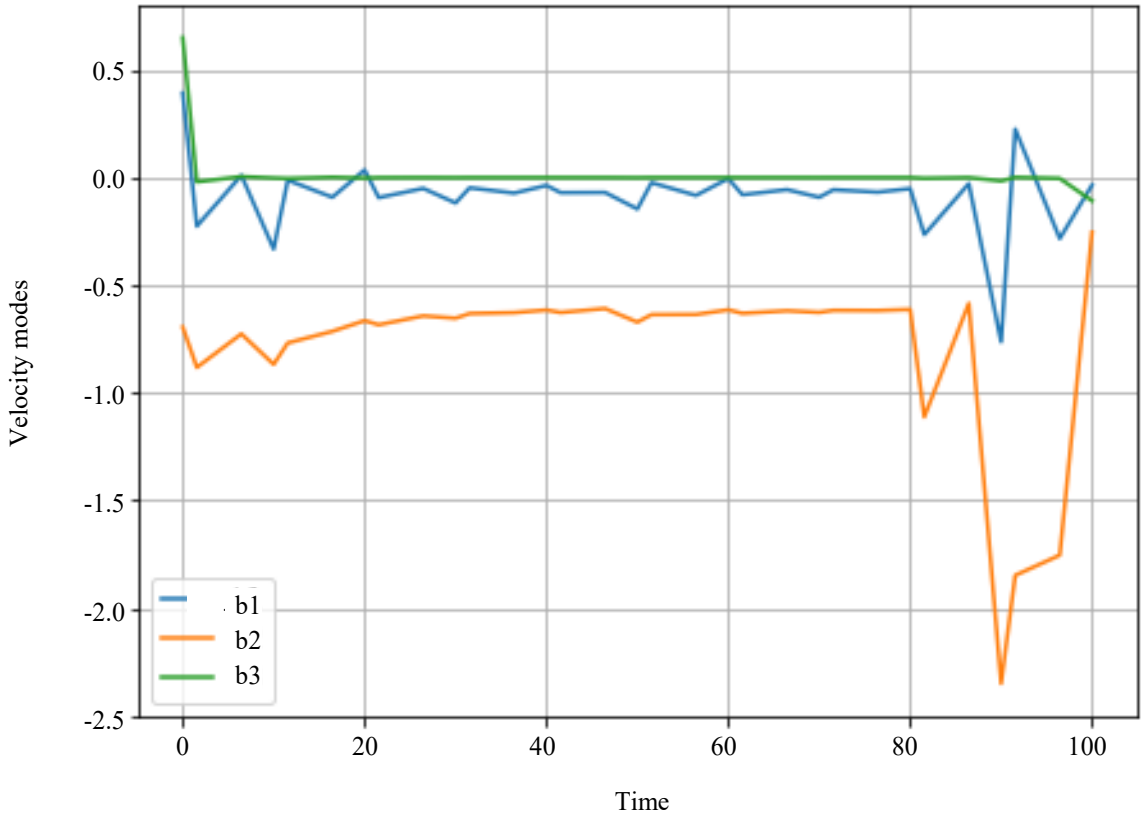



**Figure 3b.** Velocity Nodes withHopf control.

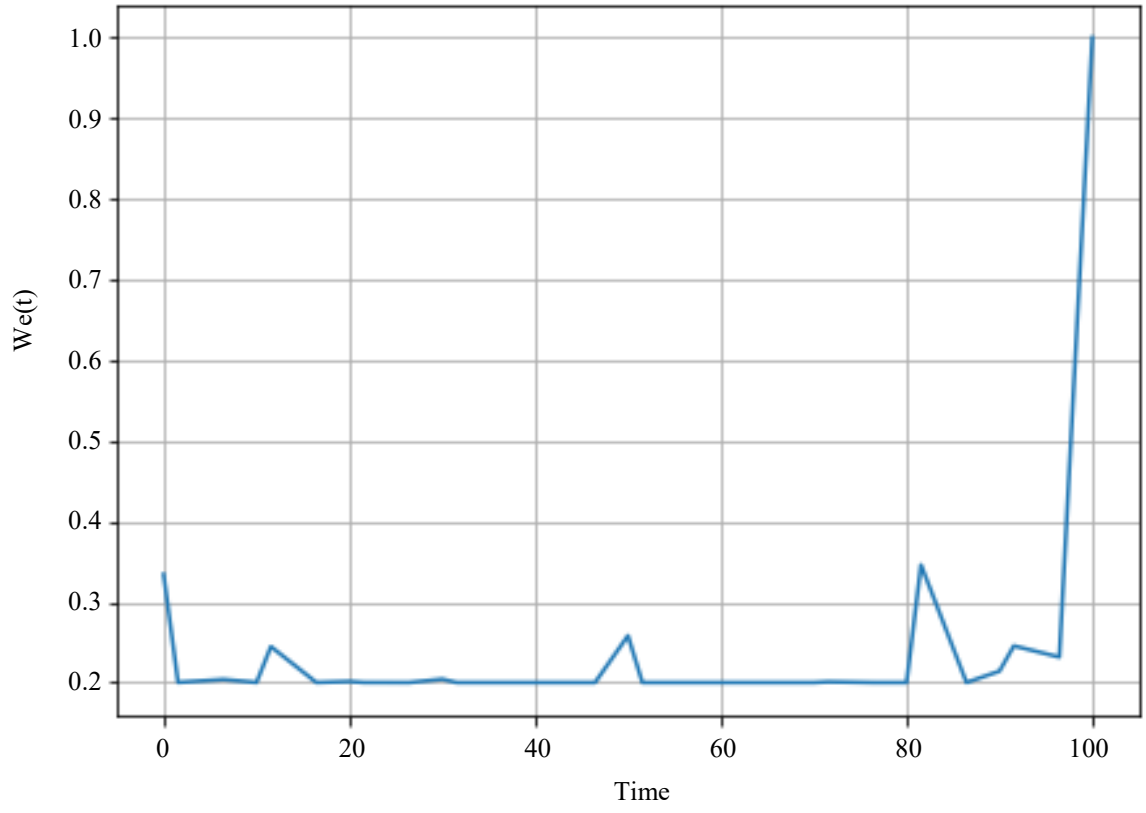



**Figure 3c.** control profile with Hopf control.

© STM Journals 2026. All Rights Reserved 

The bifurcation analysis performed using MATCONT identified a Hopf point at a critical Weber number of (We_H=0.251008), with the corresponding equilibrium state given by the modal coordinates ((a_1,a_2,a_3,b_1,b_2,b_3)=(0.141286,-4.546652,0.048410,0.391832,-0.695398,0.649639)). The appearance of a complex conjugate pair of eigenvalues crossing the imaginary axis confirms the loss of stability of the steady jet configuration. The remaining eigenvalues retain negative real parts, indicating that the instability is localized to a single oscillatory mode while the other degrees of freedom remain strongly damped. This separation of time scales is consistent with the physical interpretation of liquid jet breakup, where a dominant capillary mode grows while higher-order modes provide nonlinear saturation and energy redistribution.

The calculated first Lyapunov coefficient, (L_1=-1.110962\times10^{-2}), provides additional insight into the nature of the instability. The negative sign indicates that the Hopf bifurcation is supercritical, meaning that stable oscillations emerge continuously from the steady solution as the Weber number crosses the critical value. This behavior is physically relevant for liquid jets because breakup is generally not initiated by an abrupt transition to large-amplitude motion, but rather through the progressive amplification and nonlinear saturation of interfacial disturbances. The stable limit cycle obtained through MATCONT continuation therefore represents the nonlinear oscillatory state associated with sustained jet deformation before complete pinch-off and satellite droplet formation. The ability of the reduced-order model to reproduce this transition demonstrates that the selected Galerkin modes retain the dominant nonlinear mechanisms responsible for the instability.

A key contribution of the present work is the use of the Weber number as both a bifurcation parameter and a control variable. In conventional studies of liquid jet breakup, the Weber number is typically treated as a fixed operating condition used to classify stable and unstable regimes. Here, the Weber number is elevated from a passive descriptor of the flow regime to an active control parameter that can be dynamically manipulated. This approach provides a direct link between fundamental instability analysis and practical flow regulation. Experimentally, variations in Weber number can be achieved through modifications of the jet exit velocity, inlet pressure, flow rate, nozzle geometry, or fluid properties such as surface tension. Therefore, the optimal control formulation is not merely a mathematical stabilization strategy but represents a physically realizable mechanism for modifying the competition between inertial and capillary forces.

The optimal control results further highlight the importance of incorporating nonlinear stability information into the control design. The objective function minimizes the deviation of the Galerkin modal amplitudes from a desired steady configuration while penalizing excessive changes in the control input. Physically, this objective represents the requirement to maintain a stable jet structure while minimizing the energy or actuation effort required to achieve stabilization. Without considering the proximity of the Hopf bifurcation, the optimization problem identifies a control strategy that reduces modal deviations but does not explicitly account for the underlying stability margin of the operating state. Consequently, the optimized trajectory may approach regions where oscillatory instability can develop.

The introduction of the Hopf bifurcation avoidance constraint significantly modifies the optimal solution. The reduction in the objective function value from 6.843 without the bifurcation constraint to 3.33 with the bifurcation constraint demonstrates that incorporating nonlinear stability information improves the effectiveness of the control strategy. The approximately 49% reduction in the minimized objective indicates that the bifurcation-aware formulation provides a more favorable trajectory in the reduced-order phase space. Rather than simply minimizing instantaneous deviations, the constrained optimization actively guides the system away from unstable regions associated with oscillatory growth. This result emphasizes that stability-aware optimization can provide superior performance compared with traditional trajectory-based control approaches that neglect the underlying nonlinear dynamics.

© STM Journals 2026. All Rights Reserved 

The difference between the two control strategies can be interpreted through the phase-space structure of the reduced-order model. Without the Hopf constraint, the optimizer primarily balances state regulation and control effort. However, the nonlinear dynamics impose additional restrictions near the bifurcation boundary because small changes in the Weber number can significantly alter the eigenvalue spectrum and move the system toward oscillatory instability. By enforcing a Hopf avoidance condition, the optimization algorithm identifies regions of the parameter space where the desired state can be achieved while maintaining a finite distance from the instability threshold. This provides a more robust operating strategy for liquid jet applications where small disturbances, manufacturing variations, or environmental fluctuations may otherwise trigger breakup.

The success of the proposed approach also demonstrates the value of combining bifurcation theory with reduced-order modeling for complex free-surface flows. Direct numerical simulations of liquid jet breakup provide detailed information but are computationally expensive when embedded within optimization frameworks requiring repeated evaluations. The six-state Galerkin model developed here provides a computationally efficient alternative by retaining the dominant nonlinear physics while enabling continuation, eigenvalue analysis, and optimal control within practical computational times. Such reduced-order models are particularly valuable for real-time monitoring, digital twin development, and closed-loop control applications.

From a broader fluid mechanics perspective, the present findings contribute to the understanding of how nonlinear modal interactions influence the stability and regulation of capillary-driven flows. The emergence of a supercritical Hopf bifurcation indicates that the breakup process is preceded by a well-defined nonlinear oscillatory regime rather than occurring as an immediate transition from steady flow to fragmentation. This intermediate dynamical state provides an opportunity for intervention, where appropriately designed control strategies can modify the instability pathway before irreversible breakup occurs. The proposed framework therefore shifts the perspective from prediction of breakup after instability has developed toward proactive regulation of the instability mechanism itself.

Several extensions naturally follow from this work. Increasing the number of Galerkin modes would enable investigation of additional spatial structures involved in satellite droplet formation and nonlinear mode competition. Incorporating viscous and non-Newtonian effects would allow the framework to be applied to a broader range of industrial and biomedical fluids. Furthermore, the bifurcation-informed dataset generated from the reduced-order model provides a foundation for constructing machine-learning surrogate models capable of rapid stability prediction and adaptive control. Such hybrid physics-informed approaches could enable real-time optimization of jetting processes by combining the interpretability of dynamical systems analysis with the computational speed of data-driven models.

In summary, the results demonstrate that nonlinear reduced-order modeling, Hopf bifurcation analysis, and optimal control can be integrated into a unified framework to understand and regulate liquid jet breakup dynamics. The identification of a supercritical Hopf bifurcation, successful continuation of the resulting limit cycle, and improved performance of bifurcation-aware optimal control establish a new pathway for controlling capillary instabilities. The present methodology provides both fundamental insight into nonlinear jet dynamics and a practical computational framework for designing stable operating strategies in applications involving atomization, inkjet printing, microfluidics, and multiphase manufacturing processes.

## CONCLUSIONS

The present study developed a nonlinear Galerkin-based reduced-order model for investigating the dynamics, stability, and control of liquid jet breakup and satellite droplet formation. Starting from the incompressible Navier–Stokes equations for an axisymmetric free-surface jet, projection onto dominant Galerkin modes produced a six-state nonlinear system that retains the essential effects of inertia, surface tension, viscous dissipation, and nonlinear modal coupling while substantially reducing computational cost.

© STM Journals 2026. All Rights Reserved 

The Weber number was used as the principal bifurcation parameter. Numerical continuation identified a critical Weber number at which a complex-conjugate eigenvalue pair crossed the imaginary axis, producing a Hopf bifurcation. The negative first Lyapunov coefficient established a supercritical bifurcation and the emergence of stable limit-cycle oscillations associated with finite-amplitude jet deformation preceding satellite droplet formation.

An optimal-control formulation treated the Weber number as a physically adjustable input and minimized deviations from a desired operating state together with control effort. The resulting framework provides a practical basis for regulating jet dynamics and suppressing undesirable oscillations. Overall, the integration of reduced-order modeling, bifurcation analysis, optimal control, and data-driven stability prediction provides an efficient foundation for predictive digital twins and real-time control of liquid-jet systems. The methodology can be extended to non-axisymmetric, non-Newtonian, externally forced, and multiphase flows relevant to inkjet printing, atomization, additive manufacturing, microfluidics, and chemical processing.

## DECLARATIONS

**Acknowledgement**

Dr. Sridhar thanks Dr. Carlos Ramirez for encouraging him to write single-author papers.

**Authors Contribution**

There is only one author who did everything

**Data Availability Statement**

All data used is presented in the paper

**Conflict of interest**

The author, Dr. Lakshmi N Sridhar, has no conflict of interest.

**Funding**

No funding was obtained for this research

## REFERENCES

1. Papageorgiou DT. Analytical description of the breakup of liquid jets. J Fluid Mech. 1995;301:109-132.
2. Papageorgiou DT. On the breakup of viscous liquid threads. Phys Fluids. 1995;7(7):1529-1544.
3. Ashgriz N, Mashayek F. Temporal analysis of capillary jet breakup. J Fluid Mech. 1995;291:163-190.
4. Teng H, Kinoshita CM, Masutani SM. Prediction of droplet size from the breakup of cylindrical liquid jets. Int J Multiphase Flow. 1995;21(1):129-136.
5. Richards JR, Beris AN, Lenhoff AM. Drop formation in liquid-liquid systems before and after jetting. Phys Fluids. 1995;7(11):2617-2630.
6. Eggers J, Dupont TF. Drop formation in a one-dimensional approximation of the Navier-Stokes equation. J Fluid Mech. 1994;262:205-221.
7. Eggers J. Nonlinear dynamics and breakup of free-surface flows. Rev Mod Phys. 1997;69(3):865-929.
8. Basaran OA. Small-scale free surface flows with breakup: drop formation and emerging applications. AIChE J. 2002;48(9):1842-1848.
9. López-Herrera JM, Gañán-Calvo AM. A note on charged capillary jet breakup of conducting liquids: experimental validation of a viscous one-dimensional model. J Fluid Mech. 2004;501:303-326.
10. Notz PK, Basaran OA. Dynamics and breakup of a contracting liquid filament. J Fluid Mech. 2004;512:223-256.

© STM Journals 2026. All Rights Reserved 

11. Eggers J, Fontelos MA, Leppinen D, Snoeijer JH. Theory of the collapsing axisymmetric cavity. Physical review letters. 2007 Mar 2;98(9):094502.
12. da C Andrade EN. The velocity distribution in a liquid-into-liquid jet. Part 2: the plane jet. Proceedings of the Physical Society. 1939 Sep 1;51(5):784-93.
13. van Hoeve W, Gekle S, Snoeijer JH, Brenner MP, Versluis M, Lohse D. Breakup of diminutive Rayleigh jets. Phys Fluids. 2010;22:122003.
14. Castrejón-Pita JR, Castrejón-Pita AA, Hutchings IM. Breakup of liquid filaments. Phys Rev Lett. 2012;108:074506.
15. McIlroy C, Harlen OG. Modelling capillary breakup of particulate suspension filaments. Phys Fluids. 2014;26:033101.
16. Castrejón-Pita JR, Baxter WRS, Morgan J, Temple S, Martin GD, Hutchings IM. Future, opportunities and challenges of inkjet technologies. Atomization Sprays. 2015;25:1065-1123.
17. Hoath SD. Fundamentals of inkjet printing: the science of inkjet and droplets. Weinheim: Wiley-VCH; 2016.
18. Wang F, Tschukin O, Marques GC, Selzer M, Aghassi-Hagmann J, Nestler B. Breakup of liquid jets and the formation of satellite and subsatellite droplets. arXiv [Preprint]. 2018. Available from: https://arxiv.org/abs/1805.06818
19. Castrejón-Pita JR, Kubiak KJ, Castrejón-Pita AA, Wilson MC, Hutchings IM. Mixing and internal dynamics of droplets impacting and coalescing on a solid surface. Physical Review E—Statistical, Nonlinear, and Soft Matter Physics. 2013 Aug;88(2):023023.
20. Driessen T, Jeurissen R, Smith P, Lohse D, Versluis M. Stability of inkjet printed droplets. J Fluid Mech. 2019;863:702-725.
21. Soni SK, Kirar PK, Kolhe P, Sahu KC. Deformation and breakup of droplets in an oblique continuous air stream. Int J Multiphase Flow. 2020;122:103141.
22. Ade SS, Kirar PK, Chandrala LD, Sahu KC. Droplet size distribution in a swirl airstream using in-line holography technique. J Fluid Mech. 2023;954:A39.
23. Ade SS, Chandrala LD, Sahu KC. Size distribution of a drop undergoing breakup at moderate Weber numbers. J Fluid Mech. 2023;959:A38.
24. Srinivasan B, Sinha A. Primary breakup of liquid jet - effect of jet velocity profile. Phys Fluids. 2024;36(3).
25. Wang F, Tschukin O, Leisner T, Zhang H, Nestler B. Breakup of liquid jets: thermodynamic perspectives. arXiv [Preprint]. 2024. Available from: https://arxiv.org/abs/2402.08370
26. Dhooge A, Govaerts W, Kuznetsov YA. MATCONT: a MATLAB package for numerical bifurcation analysis of ODEs. ACM Trans Math Softw. 2003;29(2):141-164.
27. Wächter A, Biegler LT. On the implementation of an interior-point filter line-search algorithm for large-scale nonlinear programming. Math Program. 2006;106:25-57. doi:10.1007/s10107-004-0559-y.

© STM Journals 2026. All Rights Reserved 

## APPENDIX A

The dynamics of liquid jet breakup are governed by the conservation of mass and momentum together with the kinematic and dynamic conditions imposed at the deformable free surface. The present reduced-order model is derived from the incompressible Navier–Stokes equations through a sequence of physically motivated simplifications, nondimensionalization, and Galerkin projection. The objective is to obtain a low-dimensional nonlinear dynamical system that retains the dominant mechanisms responsible for capillary instability while remaining computationally efficient for bifurcation analysis and optimal control.

Consider an incompressible Newtonian liquid of density $\rho$, dynamic viscosity $\mu$, and surface tension coefficient $\sigma$ issuing from a circular nozzle of radius $R_0$. The liquid jet is assumed to be axisymmetric and surrounded by a passive gas of negligible density and viscosity. Using cylindrical coordinates $(r \mid z)$, the velocity field is expressed as $\mathbf{u} = (u_r, u_z)$, where $u_r(r,z,t)$ and $u_z(r,z,t)$ denote the radial and axial velocity components, respectively.

The governing equations consist of the incompressible continuity equation

$$\nabla \cdot \mathbf{u} = 0, \tag{25}$$

together with the Navier–Stokes momentum equation

$$\left(\frac{\partial \mathbf{u}}{\partial t} + \mathbf{u} \cdot \nabla \mathbf{u}\right) = -\nabla p + \mu \nabla^2 \mathbf{u}, \tag{26}$$

where $p(r,z,t)$ denotes the pressure field. Expressed in cylindrical coordinates, the continuity equation becomes

$$\frac{1}{r}\frac{\partial}{\partial r}(r u_r) + \frac{\partial u_z}{\partial z} = 0 \tag{27}$$

The radial momentum equation is

$$\rho\left(\frac{\partial u_r}{\partial t} + u_r \frac{\partial u_r}{\partial r} + u_z \frac{\partial u_r}{\partial z}\right) = -\frac{\partial p}{\partial r} + \mu\left[\frac{1}{r}\frac{\partial}{\partial r}\left(r \frac{\partial u_r}{\partial r}\right) + \frac{\partial^2 u_r}{\partial z^2} - \frac{u_r}{r^2}\right]. \tag{28}$$

Similarly, the axial momentum equation is

$$\rho\left(\frac{\partial u_z}{\partial t} + u_r \frac{\partial u_z}{\partial r} + u_z \frac{\partial u_z}{\partial z}\right) = -\frac{\partial p}{\partial z} + \mu[\frac{1}{r}\frac{\partial}{\partial r}\left(r \frac{\partial u_z}{\partial r}\right) + \frac{\partial^2 u_z}{\partial z^2}] \tag{29}$$

The jet interface is represented by $r = h(z,t)$, where $h(z,t)$ denotes the local jet radius. The free surface satisfies the kinematic condition

$$\frac{\partial h}{\partial t} + u_z \frac{\partial h}{\partial z} = u_r; at, r = h(z,t), \tag{30}$$

which simply states that fluid particles located on the interface remain on the interface throughout the motion.

The normal stress balance at the liquid–gas interface is

© STM Journals 2026. All Rights Reserved 

$$\mathbf{n}\cdot\mathbf{T}\cdot\mathbf{n} = -p_g + \sigma\kappa \tag{31}$$

Where

$$\mathbf{T} = -p\mathbf{I} + \mu(\nabla\mathbf{u} + \nabla\mathbf{u}^T) \tag{32}$$

is the Cauchy stress tensor, $p_g$ is the ambient gas pressure, and $\kappa$ is the interface curvature.

For an axisymmetric interface,

$$\kappa = \frac{1}{h(1+h_z^2)^{1/2}} - \frac{h_{zz}}{\left(1+h_z^2\right)^{3/2}} \tag{33}$$

where $h_z = \frac{\partial h}{\partial z}, h_{zz} = \frac{\partial^2 h}{\partial z^2}$.

The tangential stress at the free surface is assumed to vanish, $\mathbf{t}\cdot\mathbf{T}\cdot\mathbf{n} = 0,$ which is appropriate for a clean interface without surfactant effects. Although the above equations provide a complete mathematical description of the flow, they remain prohibitively expensive for repeated continuation calculations and optimal control studies. A substantial simplification is obtained by exploiting the slender geometry of the liquid jet.

The characteristic jet radius is generally much smaller than the characteristic axial wavelength of the instability. Accordingly, the aspect ratio $\partial = \frac{R_0}{L}$ satisfies $\partial \ll 1$, where $L$ denotes the characteristic axial length scale.

This assumption forms the basis of the slender-jet approximation originally introduced for capillary jet dynamics. Because radial variations occur over a much shorter length scale than axial variations, the radial velocity remains small compared with the axial velocity,

$$u_r = O\left(\partial u_z\right) \tag{34}$$

while derivatives satisfy $\frac{\partial}{\partial r} \gg \frac{\partial}{\partial z}$. Consequently, the velocity field is nearly uniform across each cross-section, permitting the governing equations to be averaged over the jet cross-sectional area.

The cross-sectional area is $A\left(z,t\right) = \pi h^2.$

Integrating the incompressibility equation over each cross-section yields the one-dimensional continuity equation

$$\frac{\partial h^2}{\partial t} + \frac{\partial}{\partial z}\left(h^2 u\right) = 0 \tag{35}$$

Where $u\left(z,t\right)$ denotes the cross-sectionally averaged axial velocity.

The one-dimensional momentum equation becomes

© STM Journals 2026. All Rights Reserved 

$$\frac{\partial u}{\partial t}+u\frac{\partial u}{\partial z}=-\frac{\partial p_c}{\partial z}+\frac{3\mu}{\rho h^2}\frac{\partial}{\partial z}\left(h^2\frac{\partial u}{\partial z}\right) \tag{36}$$

Where $p_c=\sigma\kappa$ represents the capillary pressure. The slender-jet approximation also simplifies the curvature expression. Since $|h_z|\square\ 1,$ the curvature can be expanded as

$$\kappa=\frac{1}{h}-h_{zz}+O\left(\dot{o}^2\right) \tag{37}$$

Neglecting higher-order terms gives

$$\kappa\approx\frac{1}{h}-h_{zz}. \tag{38}$$

Accordingly,

$$p_c=\sigma(\frac{1}{h}-h_{zz}). \tag{39}$$

Substitution into the momentum equation produces

$$\frac{\partial u}{\partial t}+u\frac{\partial u}{\partial z}=-\frac{\sigma}{\rho}\frac{\partial}{\partial z}(\frac{1}{h}-h_{zz})+\frac{3\mu}{\rho h^2}\frac{\partial}{\partial z}\left(h^2\frac{\partial u}{\partial z}\right) \tag{40}$$

The equations are now written entirely in terms of the jet radius and the cross-sectionally averaged velocity.

To identify the dominant dimensionless parameters governing the instability, the equations are nondimensionalized using the characteristic scales $R_0$ for length, $U_0$. for velocity,and $\frac{R_0}{U_0}$ for time.

The nondimensional variables are introduced as $z=R_0z^*,\quad h=R_0h^*,\ u=U_0u^*,$ $t=\frac{R_0}{U_0}t^*,$ and $p=\rho U_0^2p^*.$

Substituting these relations into the governing equations and dividing by the appropriate characteristic scales yields the nondimensional continuity equation

$$\frac{\partial h^2}{\partial t}+\frac{\partial}{\partial z}\left(h^2u\right)=0 \tag{41}$$

and the nondimensional momentum equation

$$\frac{\partial u}{\partial t}+u\frac{\partial u}{\partial z}=-\frac{1}{We}\frac{\partial}{\partial z}(\frac{1}{h}-h_{zz})+\frac{3}{Re\,h^2}\frac{\partial}{\partial z}\left(h^2\frac{\partial u}{\partial z}\right), \tag{42}$$

where the Reynolds number and Weber number are defined as $Re=\frac{\rho U_0R_0}{\mu}$, and $We=\frac{\rho U_0^2R_0}{\sigma}$ .

The Weber number measures the ratio of inertial forces to capillary forces and therefore governs the onset of capillary instability. In the present work, it is selected as the principal bifurcation parameter because variations in $We$ directly modify the balance between inertia and surface tension, thereby determining whether disturbances decay or evolve into finite-amplitude oscillations leading to jet

© STM Journals 2026. All Rights Reserved 

breakup.

The nondimensional equations derived previously describe the evolution of the jet radius and the cross-sectionally averaged axial velocity as continuous functions of space and time. Although these equations are substantially simpler than the original Navier–Stokes equations, they still constitute an infinite-dimensional dynamical system because both the interface radius and the velocity field depend continuously on the axial coordinate. The objective of the Galerkin procedure is to approximate these distributed fields using a finite number of dominant spatial modes so that the governing partial differential equations are transformed into a low-dimensional system of nonlinear ordinary differential equations while retaining the principal physical mechanisms responsible for jet instability.The steady base state of the jet corresponds to a cylindrical liquid column of uniform radius moving with constant axial velocity. In nondimensional form, the steady solution is $h_0(z)=1,$ and $u_0(z)=1.$

The stability of this equilibrium is investigated by introducing perturbations about the steady state. The instantaneous jet radius is therefore written as

$$h(z,t)=1+\eta(z,t) \tag{43}$$

where $\eta(z,t)$ represents the interface deformation. Similarly, the axial velocity is expressed as

$$u(z,t)=1+v(z,t) \tag{44}$$

where $v(z,t)$ denotes the perturbation velocity field.The disturbances are assumed to remain sufficiently smooth so that both fields admit convergent modal expansions. The Galerkin approximation seeks the disturbance fields in the form

$$\eta(z,t)=\sum_{i=1}^{N} a_i(t)\phi_i(z) \tag{45}$$

and

$$v(z,t)=\sum_{i=1}^{N} b_i(t)\phi_i(z) \tag{46}$$

where $a_i(t)$ are the modal amplitudes describing the interface deformation, $b_i(t)$ are the modal amplitudes describing the velocity perturbation,and $\phi_i(z)$ are prescribed spatial basis functions satisfying the boundary conditions of the computational domain.

For the present reduced-order model only the first three dominant modes are retained, giving

$$\eta(z,t)=a_1(t)\phi_1(z)+a_2(t)\phi_2(z)+a_3(t)\phi_3(z) \tag{47}$$

And

$$v(z,t)=b_1(t)\phi_1(z)+b_2(t)\phi_2(z)+b_3(t)\phi_3(z) \tag{48}$$

The corresponding approximation for the complete jet radius becomes

$$h(z,t)=1+a_1\phi_1+a_2\phi_2+a_3\phi_3 \tag{49}$$

while the axial velocity field is

© STM Journals 2026. All Rights Reserved 

$$u(z,t) = 1 + b_1\phi_1 + b_2\phi_2 + b_3\phi_3 \tag{50}$$

The basis functions are assumed to satisfy the orthogonality condition

$$\int_0^L \phi_i(z)\,\phi_j(z)\,dz = 0, i \neq j, \tag{51}$$

and are normalized such that $\int_0^L \phi_i^2(z)\,dz = 1$. A convenient choice consists of trigonometric eigenfunction $\phi_i(z) = \sin\left(\frac{i\pi z}{L}\right)$, although other orthogonal bases, including Legendre or Chebyshev polynomials, may also be employed. The present derivation remains independent of the specific basis and therefore applies generally to any complete orthogonal set. The temporal derivatives of the modal expansions are obtained by differentiating only the modal amplitudes since the basis functions are independent of time. Consequently,

$$\frac{\partial \eta}{\partial t} = \frac{da_1}{dt}\phi_1 + \frac{da_2}{dt}\phi_2 + \frac{da_3}{dt}\phi_3 \tag{52}$$

and

$$\frac{\partial v}{\partial t} = \frac{db_1}{dt}\phi_1 + \frac{db_2}{dt}\phi_2 + \frac{db_3}{dt}\phi_3 \tag{53}$$

Spatial derivatives are similarly obtained as

$$\begin{aligned}
\frac{\partial \eta}{\partial z} &= a_1\phi_1' + a_2\phi_2' + a_3\phi_3' \\
\frac{\partial^2 \eta}{\partial z^2} &= a_1\phi_1'' + a_2\phi_2'' + a_3\phi_3'' \\
\frac{\partial v}{\partial z} &= b_1\phi_1' + b_2\phi_2' + b_3\phi_3', \\
\frac{\partial^2 v}{\partial z^2} &= b_1\phi_1'' + b_2\phi_2'' + b_3\phi_3''
\end{aligned} \tag{54}$$

The nonlinear terms appearing in the governing equations are next expanded in terms of the modal amplitudes. The square of the interface radius is

$$h^2 = (1+\eta)^2 = 1 + 2\eta + \eta^2 \tag{55}$$

Since $\eta = a_1\phi_1 + a_2\phi_2 + a_3\phi_3$, the quadratic contribution becomes

$$\eta^2 = a_1^2\phi_1^2 + a_2^2\phi_2^2 + a_3^2\phi_3^2 + 2a_1a_2\phi_1\phi_2 + 2a_1a_3\phi_1\phi_3 + 2a_2a_3\phi_2\phi_3 \tag{56}$$

Similarly,

$$h^2u = \left(1 + 2\eta + \eta^2\right)(1+v) \tag{57}$$

Neglecting cubic and higher-order products gives

$$h^2u \approx 1 + 2\eta + v + \eta^2 + 2\eta v \tag{58}$$

© STM Journals 2026. All Rights Reserved 

The quadratic interaction term is

$$2\eta v = 2\left(a_1\phi_1 + a_2\phi_2 + a_3\phi_3\right)\left(b_1\phi_1 + b_2\phi_2 + b_3\phi_3\right) \tag{59}$$

Expanding this product yields

$$\begin{aligned} 2\eta v = \quad & 2a_1b_1\phi_1^2 + 2a_2b_2\phi_2^2 + 2a_3b_3\phi_3^2 \\ & +2\left(a_1b_2 + a_2b_1\right)\phi_1\phi_2 \\ & +2\left(a_1b_3 + a_3b_1\right)\phi_1\phi_3 \\ & +2\left(a_2b_3 + a_3b_2\right)\phi_2\phi_3. \end{aligned} \tag{60}$$

The reciprocal radius appearing in the capillary pressure is expanded using a Taylor series. Since $h = 1 + \eta,$

the reciprocal becomes

$$\frac{1}{h} = (1+\eta)^{-1} \tag{61}$$

Expanding about the steady cylindrical state gives

$$\frac{1}{h} = 1 - \eta + \eta^2 - \eta^3 + \cdots \tag{62}$$

Retaining terms through quadratic order,

$$\frac{1}{h} \approx 1 - \eta + \eta^2 \tag{63}$$

Likewise,

$$h_{zz} = a_1\phi_1'' + a_2\phi_2'' + a_3\phi_3'' \tag{64}$$

The capillary pressure therefore becomes

$$p_c = \frac{1}{We}\left(\frac{1}{h} - h_{zz}\right) \tag{65}$$

Or

$$p_c = \frac{1}{We}\left[1 - \eta + \eta^2 - a_1\phi_1'' - a_2\phi_2'' - a_3\phi_3''\right] \tag{66}$$

Differentiating with respect to the axial coordinate gives

$$\frac{\partial p_c}{\partial z} = \frac{1}{We}\left[-\frac{\partial \eta}{\partial z} + \frac{\partial\left(\eta^2\right)}{\partial z} - \frac{\partial h_{zz}}{\partial z}\right] \tag{67}$$

The viscous contribution is written as $\frac{3}{Re\,h^2}\frac{\partial}{\partial z}\left(h^2\frac{\partial u}{\partial z}\right)$. Using $h^2 = 1 + 2\eta + \eta^2,$ and neglecting cubic terms,

$$h^2\frac{\partial u}{\partial z} = \left(1 + 2\eta + \eta^2\right)\left(b_1\phi_1' + b_2\phi_2' + b_3\phi_3'\right). \tag{68}$$

© STM Journals 2026. All Rights Reserved 

Differentiation with respect to the axial coordinate generates both linear viscous diffusion terms and nonlinear coupling terms involving products of the modal amplitudes. These nonlinear interactions provide the mechanism through which energy is transferred between different deformation modes and play an essential role in the saturation of the capillary instability. Substitution of all modal expansions into the nondimensional continuity and momentum equations produces residual equations that depend only on the modal amplitudes and the spatial basis functions. Because the Galerkin approximation cannot satisfy the governing partial differential equations exactly with a finite number of modes, a residual remains after substitution. The Galerkin method determines the modal amplitudes by requiring this residual to be orthogonal to each basis function over the computational domain. This weighted residual formulation forms the foundation of the reduced-order model and, in the following derivation, is used to transform the governing partial differential equations into the six coupled nonlinear ordinary differential equations describing the evolution of the Galerkin modal amplitudes.

The substitution of the Galerkin expansions into the governing equations transforms the distributed free-surface problem into a system of residual equations. The remaining task is to determine the unknown modal amplitudes by requiring these residuals to be orthogonal to the chosen basis functions. This procedure is known as the Galerkin weighted-residual method and ensures that the approximation minimizes the projection error over the solution domain.

After substitution of the modal expansions into the continuity equation,

$$\frac{\partial h^2}{\partial t}+\frac{\partial}{\partial z}\left(h^2 u\right)=0 \tag{69}$$

a residual function is obtained,

$$R_c\left(z,t\right)=\frac{\partial h^2}{\partial t}+\frac{\partial}{\partial z}\left(h^2 u\right) \tag{70}$$

Since only three spatial modes are retained, the residual cannot vanish identically for every value of the spatial coordinate. Instead, the Galerkin approximation requires

$$R_c\left(z,t\right)=\frac{\partial h^2}{\partial t}+\frac{\partial}{\partial z}\left(h^2 u\right) \tag{71}$$

These three equations determine the evolution of the interface amplitudes.

The first contribution arises from the temporal derivative of the interface area, $\frac{\partial h^2}{\partial t}=2h\frac{\partial h}{\partial t}$. Substituting $h=1+\eta,$ gives

$$\frac{\partial h^2}{\partial t}=2\left(1+\eta\right)\frac{\partial \eta}{\partial t} \tag{72}$$

Using the modal expansion,

$$\frac{\partial \eta}{\partial t}=\frac{da_1}{dt}\phi_1+\frac{da_2}{dt}\phi_2+\frac{da_3}{dt}\phi_3 \tag{73}$$

Yields

$$\frac{\partial h^2}{\partial t}=2\left(1+\eta\right)\left(\frac{da_1}{dt}\phi_1+\frac{da_2}{dt}\phi_2+\frac{da_3}{dt}\phi_3\right). \tag{74}$$

Neglecting cubic products,

© STM Journals 2026. All Rights Reserved 

$$\frac{\partial h^2}{\partial t} \approx 2\left(\frac{da_1}{dt}\phi_1 + \frac{da_2}{dt}\phi_2 + \frac{da_3}{dt}\phi_3\right) + 2\eta\left(\frac{da_1}{dt}\phi_1 + \frac{da_2}{dt}\phi_2 + \frac{da_3}{dt}\phi_3\right) \tag{75}$$

The convective contribution is $\frac{\partial}{\partial z}\left(h^2 u\right)$. Since $h^2 u = 1 + 2\eta + v + \eta^2 + 2\eta v,$ differentiation gives

$$\frac{\partial\left(h^2 u\right)}{\partial z} = 2\frac{\partial \eta}{\partial z} + \frac{\partial v}{\partial z} + \frac{\partial\left(\eta^2\right)}{\partial z} + 2\frac{\partial(\eta v)}{\partial z} \tag{76}$$

=

The derivatives become

$$\begin{aligned} \frac{\partial \eta}{\partial z} &= a_1\phi_1^{'} + a_2\phi_2^{'} + a_3\phi_3^{'} \\ \frac{\partial v}{\partial z} &= b_1\phi_1^{'} + b_2\phi_2^{'} + b_3\phi_3^{'} \end{aligned} \tag{77}$$

The derivative of the quadratic deformation term is $\frac{\partial\left(\eta^2\right)}{\partial z} = 2\eta\frac{\partial \eta}{\partial z}$, which introduces products such as

$a_1a_2, a_1a_3, a_2a_3,$ representing nonlinear interaction between deformation modes. Similarly,

$$\frac{\partial(\eta v)}{\partial z} = \eta\frac{\partial v}{\partial z} + v\frac{\partial \eta}{\partial z} \tag{78}$$

which generates additional nonlinear coupling between interface deformation and velocity. The weighted residual equation for the first mode therefore becomes $\int_0^L R_c\phi_1\, dz = 0.$

After substitution,

$$\int_0^L 2\frac{da_1}{dt}\phi_1^2\, dz + \int_0^L 2\eta\frac{da_1}{dt}\phi_1^2\, dz + \int_0^L 2\frac{\partial \eta}{\partial z}\phi_1\, dz + \int_0^L \frac{\partial v}{\partial z}\phi_1\, dz + \int_0^L 2\eta\frac{\partial \eta}{\partial z}\phi_1\, dz 2\int_0^L \frac{\partial(\eta v)}{\partial z}\phi_1\, dz = 0 \tag{79}$$

The orthogonality of the basis functions eliminates all cross products involving different modes, $\int_0^L \phi_i\phi_j\, dz = 0, i \neq j,$ leaving only the dominant modal interactions. Introducing the Galerkin coefficients $\alpha_1 = -\int_0^L \phi_1^{'}\phi_1\, dz,$ and $\beta_1 = \int_0^L \phi_1^2\phi_2\, dz,$ the projected continuity equation reduces to

$$\frac{da_1}{dt} = b_1 - \alpha_1 a_1 + \beta_1 a_1 a_2 \tag{80}$$

The first term represents the kinematic relationship between interface displacement and velocity.The second term originates from viscous damping of the interface deformation.The quadratic interaction term arises from nonlinear deformation of the free surface and represents the transfer of energy between the first and second Galerkin modes.Projection onto the second basis function follows the same procedure,

© STM Journals 2026. All Rights Reserved 

$$\int_0^L R_c \phi_2 \, dz = 0 \tag{81}$$

Evaluation of the projection integrals produces

$$\frac{da_2}{dt} = b_2 - \alpha_2 a_2 + \beta_2 a_1^2 + \gamma_2 a_1 a_3 \tag{82}$$

where $\alpha_2 = -\int_0^L \phi_2' \phi_2 \, dz$, $\beta_2 = \int_0^L \phi_2 \phi_1^2 \, dz$, and $\gamma_2 = \int_0^L \phi_1 \phi_2 \phi_3 \, dz$.

The coefficient $\beta_2$ describes the quadratic self-interaction of the dominant instability mode. The mixed coefficient

$\gamma_2$ accounts for the transfer of energy between the first and third deformation modes through the second mode.

Repeating the projection for the third basis function, $\int_0^L R_c \phi_3 \, dz = 0$, yields

$$\frac{da_3}{dt} = b_3 - \alpha_3 a_3 + \beta_3 a_1 a_2 \tag{83}$$

where $\alpha_3 = -\int_0^L \phi_3' \phi_3 \, dz$, and $\beta_3 = \int_0^L \phi_1 \phi_2 \phi_3 \, dz$.

The three projected continuity equations therefore become

$$\begin{aligned} \frac{da_1}{dt} &= b_1 - \alpha_1 a_1 + \beta_1 a_1 a_2 \\ \frac{da_2}{dt} &= b_2 - \alpha_2 a_2 + \beta_2 a_1^2 + \gamma_2 a_1 a_3 \\ \frac{da_3}{dt} &= b_3 - \alpha_3 a_3 + \beta_3 a_1 a_2 \end{aligned} \tag{84}$$

These equations constitute the kinematic component of the reduced-order model and describe the temporal evolution of the interface deformation modes. The linear terms represent viscous attenuation of each deformation mode, whereas the quadratic terms arise directly from the nonlinear geometry of the free surface and describe the exchange of energy between interacting instability modes. The velocity amplitudes act as generalized modal velocities that couple the continuity and momentum equations. In the following derivation, the Galerkin projection is applied to the momentum equation to obtain the remaining three ordinary differential equations governing the evolution of the velocity modes, thereby completing the six-state nonlinear reduced-order model.

The remaining three ordinary differential equations are obtained by projecting the nondimensional momentum equation onto the same Galerkin basis functions. The momentum equation governing the cross-sectionally averaged velocity is

© STM Journals 2026. All Rights Reserved 

$$\frac{\partial u}{\partial t}+u\frac{\partial u}{\partial z}=-\frac{1}{We}\frac{\partial}{\partial z}(\frac{1}{h}|h_{zz})+\frac{3}{Reh^2}\frac{\partial}{\partial z}\left(h^2\frac{\partial u}{\partial z}\right) \tag{85}$$

Following substitution of the modal expansions,

$$\begin{aligned} u&=1+b_1\phi_1+b_2\phi_2+b_3\phi_3\\ h&=1+a_1\phi_1+a_2\phi_2+a_3\phi_3 \end{aligned} \tag{86}$$

a momentum residual is obtained,

$$R_m\left(z,t\right)=\frac{\partial u}{\partial t}+u\frac{\partial u}{\partial z}+\frac{1}{We}\frac{\partial}{\partial z}(\frac{1}{h}-h_{zz})-\frac{3}{Reh^2}\frac{\partial}{\partial z}\left(h^2\frac{\partial u}{\partial z}\right) \tag{87}$$

The Galerkin approximation requires the momentum residual to be orthogonal to every basis function,

$$\int_0^L R_m\left(z,t\right)\phi_i\left(z\right)dz=0, i=1,2,3 \tag{88}$$

The first contribution is the temporal acceleration,

$$\frac{\partial u}{\partial t}=\frac{db_1}{dt}\phi_1+\frac{db_2}{dt}\phi_2+\frac{db_3}{dt}\phi_3. \tag{89}$$

Projection immediately generates the generalized inertia terms, $\frac{db_i}{dt}, i=1,2,3.$ The nonlinear convective contribution is $u\frac{\partial u}{\partial z}.$ Substituting the modal expansion gives $(1+b_1\phi_1+b_2\phi_2+b_3\phi_3)\left(b_1\phi_1^{'}+b_2\phi_2^{'}+b_3\phi_3^{'}\right).$

Expanding the product yields

$$\begin{aligned} u\frac{\partial u}{\partial z}&=b_1\phi_1^{'}+b_2\phi_2^{'}+b_3\phi_3^{'}+b_1^2\phi_1\phi_1^{'}+b_2^2\phi_2\phi_2^{'}+b_3^2\phi_3\phi_3^{'}+\\ &b_1b_2\left(\phi_1\phi_2^{'}+\phi_2\phi_1^{'}\right)+b_1b_3\left(\phi_1\phi_3^{'}+\phi_3\phi_1^{'}\right)+b_2b_3\left(\phi_2\phi_3^{'}+\phi_3\phi_2^{'}\right) \end{aligned} \tag{90}$$

These quadratic products represent nonlinear momentum transport and provide one of the principal mechanisms responsible for energy transfer among the dominant instability modes.

The capillary contribution follows from $-\frac{1}{We}\frac{\partial}{\partial z}(\frac{1}{h}-h_{zz}).$ Using the expansion $\frac{1}{h}=1-\eta+\eta^2,$ together with $\eta=a_1\phi_1+a_2\phi_2+a_3\phi_3,$ gives

$$\frac{\partial}{\partial z}(\frac{1}{h}-h_{zz})=-\eta_z+2\eta\eta_z-\eta_{zzz} \tag{91}$$

The first term corresponds to the linear capillary restoring force, while the remaining terms represent nonlinear curvature effects associated with finite interface deformation.Projection of these terms produces restoring forces proportional to the modal amplitudes, $-\omega_i^2a_i,$ where

© STM Journals 2026. All Rights Reserved 

$$\omega_i^2 = \frac{1}{We}\int_0^L \phi_i(\phi_i''' - \phi_i')dz \tag{92}$$

The quantities $\omega_i$ may therefore be interpreted as the natural frequencies of the Galerkin modes arising from capillary wave propagation.The viscous contribution is $\frac{3}{Re\,h^2}\frac{\partial}{\partial z}\left(h^2\frac{\partial u}{\partial z}\right)$.

Expanding $h^2 = 1 + 2\eta + \eta^2$, and retaining quadratic terms gives $\frac{3}{Re}\left[\frac{\partial^2 u}{\partial z^2} + 2\eta\frac{\partial^2 u}{\partial z^2} + 2\eta_z\frac{\partial u}{\partial z}\right]$.

Projection onto each basis function produces two distinct classes of terms.The first class generates linear damping,

$-\zeta_i b_i$, where $\zeta_i = -\frac{3}{Re}\int_0^L \phi_i\phi_i''dz$. These coefficients represent viscous dissipation of kinetic energy.The second class contains products between deformation amplitudes and velocity amplitudes, $a_i b_j$,

which arise because viscosity depends on the evolving jet geometry. These terms represent nonlinear coupling between interface deformation and velocity and are expressed as

$$\eta_i = \frac{3}{Re}\int_0^L \phi_i\phi_j\phi_k''dz \tag{93}$$

The resulting nonlinear viscous interaction appears as $\eta_1 a_2 b_1$, $\eta_2 a_1 b_2$, and $\eta_3 a_2 b_3$. These coupling terms describe the modulation of viscous damping by the evolving interface deformation and become increasingly important as the oscillation amplitude grows.

Finally, the steady base flow contributes a constant forcing term obtained from the projection of the equilibrium momentum balance,

$$F = \int_0^L S(z)\phi_1(z)dz, \tag{94}$$

where $S(z)$ represents the forcing associated with the imposed inlet flow conditions.

Collecting all projected contributions for the first velocity mode gives

$$\frac{db_1}{dt} = -\omega_1^2 a_1 - \zeta_1 b_1 + \frac{1}{We}(a_1 - a_1^3) + \eta_1 a_2 b_1 + F \tag{95}$$

The first term represents the capillary restoring force, the second term viscous dissipation, the third term nonlinear capillary saturation, the fourth term nonlinear viscous coupling, and the final term the external forcing generated by the mean flow.Applying the same projection procedure to the second mode yields

$$\frac{db_2}{dt} = -\omega_2^2 a_2 - \zeta_2 b_2 + \frac{1}{We}(a_2 - a_1^2) + \eta_2 a_1 b_2 \tag{96}$$

=

Similarly, projection onto the third basis function gives

© STM Journals 2026. All Rights Reserved 

$$\frac{db_3}{dt} = -\omega_3^2 a_3 - \zeta_3 b_3 + \frac{1}{We}(a_3 - a_1 a_2) + \eta_3 a_2 b_3 \tag{97}$$

$$=$$ `

Combining these three equations with the three equations derived from the continuity equation produces the complete six-state reduced-order model,

$$\begin{aligned}
\frac{da_1}{dt} &= b_1 - \alpha_1 a_1 + \beta_1 a_1 a_2 \\
\frac{da_2}{dt} &= b_2 - \alpha_2 a_2 + \beta_2 a_1^2 + \gamma_2 a_1 a_3 \\
\frac{da_3}{dt} &= b_3 - \alpha_3 a_3 + \beta_3 a_1 a_2 \\
\frac{db_1}{dt} &= -\omega_1^2 a_1 - \zeta_1 b_1 + \frac{1}{We}(a_1 - a_1^3) + \eta_1 a_2 b_1 + F \\
\frac{db_2}{dt} &= -\omega_2^2 a_2 - \zeta_2 b_2 + \frac{1}{We}(a_2 - a_1^2) + \eta_2 a_1 b_2 \\
\frac{db_3}{dt} &= -\omega_3^2 a_3 - \zeta_3 b_3 + \frac{1}{We}(a_3 - a_1 a_2) + \eta_3 a_2 b_3
\end{aligned} \tag{98}$$

The resulting system constitutes a nonlinear six-dimensional dynamical representation of the dominant capillary instability mechanisms governing liquid jet breakup. The first three equations describe the kinematic evolution of the interface deformation modes, while the remaining three equations describe the corresponding momentum balance for the modal velocities. The linear terms account for capillary restoration and viscous damping, whereas the quadratic and cubic terms originate from the nonlinear geometry of the free surface, convective momentum transport, and mode-to-mode energy exchange generated during the Galerkin projection. Consequently, the reduced-order model preserves the essential physical mechanisms responsible for the growth, saturation, and interaction of capillary instability modes while reducing the original infinite-dimensional free-surface problem to a computationally efficient six-state system suitable for nonlinear stability analysis and prediction of liquid jet oscillations preceding satellite droplet formation.

The use of Galerkin projection is motivated by its ability to preserve the dominant physical mechanisms governing liquid jet dynamics while substantially reducing the computational complexity of the original free-surface problem. Rather than attempting to resolve the complete infinite-dimensional governing equations, the Galerkin approach projects the dynamics onto a finite set of physically meaningful spatial modes that capture the dominant capillary and inertial behavior. Such reduced-order models have been widely employed in fluid mechanics because they retain the essential nonlinear mode interactions responsible for the system dynamics while providing a computationally efficient framework for parametric studies, stability analysis, and control-oriented investigations. The objective of the present work is therefore not to replace high-fidelity numerical simulations, but to develop a physically interpretable low-dimensional model that reproduces the dominant dynamics preceding liquid jet breakup and serves as a foundation for nonlinear dynamical systems analysis.

© STM Journals 2026. All Rights Reserved 